JOURNAL OF GEOPHYSICAL RESEARCH, VOL. 112, A11312, doi:10.1029/2007JA012407, 2007

Modeling elves observed by FORMOSAT-2 satellite

Cheng-Ling Kuo,[1,2] A. B. Chen,[1] Y. J. Lee,[1] L. Y. Tsai,[1] R. K. Chou,[1] R. R. Hsu,[1] H. T. Su,[1] L. C. Lee,[2] S. A. Cummer,[3] H. U. Frey,[4] S. B. Mende,[4] Y. Takahashi,[5] and H. Fukunishi[5]

Received 18 March 2007; revised 20 July 2007; accepted 31 July 2007; published 22 November 2007.

[1] The ISUAL experiment on the FORMOSAT-2 satellite has confirmed the existence of ionization and Lyman-Birge-Hopfield (LBH) band emissions in elves. In this paper, an in-depth study of the ISUAL recorded elves was carried out. Numerical simulation results of elves based on an electromagnetic finite difference time domain (FDTD) model of the emissions between 185–800 nm and of their spatial-temporal evolution are presented. To account for the effect of atmospheric attenuation, three major attenuation mechanisms: O_2, O_3, and molecular Rayleigh scattering are considered. Validations of the electromagnetic FDTD model were conducted in three ways: by comparing the calculated and observed photon fluxes in the ISUAL spectrophotometric channels, by directly comparing the simulated and observed morphologies of elves, and by comparing the computed photon counts of the ISUAL Imager based on the derived peak currents for two elve-associated NLDN (National Lightning Detection Network) cloud-to-ground discharges (CGs) with those recorded by the ISUAL Imager. In all three ways, very good agreement was achieved.

Citation: Kuo, C.-L., et al. (2007), Modeling elves observed by FORMOSAT-2 satellite, *J. Geophys. Res.*, *112*, A11312, doi:10.1029/2007JA012407.

1. Introduction

[2] Thunderstorm-related optical flashes in the lower ionosphere and middle atmosphere are categorized into several types of transient luminous events (TLEs), including sprites [*Franz et al.*, 1990; *Sentman et al.*, 1995; *Pasko et al.*, 1997; *Su et al.*, 2002], elves [*Inan et al.*, 1991; *Boeck et al.*, 1992; *Fukunishi et al.*, 1996], blue jets and gigantic jets [*Wescott et al.*, 1995; *Pasko et al.*, 2002; *Su et al.*, 2003]. Elves were first discovered in the space shuttle images [*Boeck et al.*, 1992] and were subsequently identified from ground observations using high-speed photometry [*Fukunishi et al.*, 1996]. The cause of elves is believed to be heating of the electrons by the electromagnetic pulses (EMPs) emitted from cloud-to-ground discharges [*Inan et al.*, 1996; *Fernsler and Rowland*, 1996; *Barrington-Leigh and Inan*, 1999; *Veronis et al.*, 1999]. The *E* field driven electrons collide with molecular nitrogen and molecular oxygen, inducing excitation and/or ionization and eventually resulting in the expanding luminous emissions in the lower ionosphere. The typical altitude of elves is in the range of 80–95 km and their lateral dimension is 200–500 km. The short luminous duration (~1 ms) and the severe atmospheric attenuation of short-wavelength emissions have limited the success in obtaining the full spectroscopic information of elves from ground observations. For example, several high-speed (~60 kHz) photomultiplier-based photometric measurements of elves [*Inan et al.*, 1997; *Barrington-Leigh and Inan*, 1999] have been performed, but the full band emissions of elves, especially in the UV and FUV bands, have not been resolved.

[3] Recently, the ISUAL experiment on FORMOSAT-2 satellite has confirmed the existence of ionization and Lyman-Birge-Hopfield (LBH) band emissions in elves [*Mende et al.*, 2005]. This exciting result demonstrated the advantage of space-borne observation platform. Here we report in-depth numerical simulations based on an electromagnetic finite difference time domain (FDTD) model to elucidate the observed characteristics of the ISUAL elves. An electromagnetic FDTD model has been used to in the past to explain the morphologies and to predict the photometric behavior of ground-observed elves [*Inan et al.*, 1997; *Pasko et al.*, 1998; *Barrington-Leigh and Inan*, 1999; *Veronis et al.*, 1999]. In this paper, a similar electromagnetic FDTD model was employed to predict the elves emissions between 185–800 nm, to project the spatial-temporal evolution, to explain the morphology and to elucidate the photometric behavior of the ISUAL recorded elves. The numerical study includes an electric current which flows in the conducting channel of a cloud-to-

[1]Department of Physics, National Cheng Kung University, Tainan, Taiwan.
[2]Institute of Space Science, National Central University, Jhongli, Taiwan.
[3]Electrical and Computer Engineering Department, Duke University, Durham, North Carolina, USA.
[4]Space Sciences Laboratory, University of California, Berkeley, California, USA.
[5]Department of Geophysics, Tohoku University, Sendai, Japan.

0148-0227/07/2007JA012407$09.00

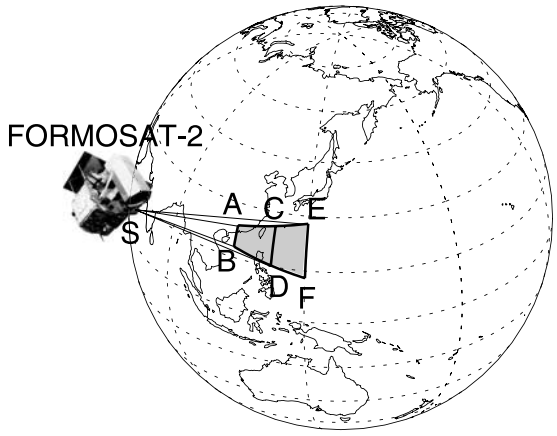

Figure 1. Observational configuration of the ISUAL instruments onboard the FORMOSAT-2 satellite (labeled as "S"). The FOV of ISUAL Imager and SP cover a region of nearly two million square kilometers on Earth's surface (gray area).

ground lighting for an extended period. This nearly impulsive current radiates an electromagnetic dipole field, whose strength at the lower ionosphere can be computed via the Maxwell equations and a coupled electron density continuity equation. The E field–energized electrons impact, excite, or ionize the ambient molecular nitrogen and oxygen, which subsequently emit the observed luminous emissions.

2. ISUAL Experiment

[4] The elves data presented in this paper were recorded by the ISUAL payload on FORMOSAT-2 satellite [*Chern et al.*, 2003]. FORMOSAT-2 is a Sun-synchronous satellite which is capable of surveying the whole globe with 14 daily revisiting orbits. The ISUAL payload consists of an ICCD Imager, a six-channel spectrophotometer (SP) and an array photometer (AP). The Imager data were obtained through a 623–750 nm filter with an image frame integration time of 14 ms. The key SP data are from channel 2 (centered at 337 nm; bandwidth 5.6 nm) and channel 3 (centered at 391.4 nm; bandwidth 4.2 nm) of the ISUAL SP. Other SP channels include SP1 (150–290 nm), SP4 (608.9–753.4 nm), SP5 (centered at 777.4 nm), and SP6 (228.2–410.2 nm). The sampling rate of the ISUAL SP is 10 kHz. The ISUAL AP contains a blue (370–450 nm) and a red (530–650 nm) band multiple-anode photometers. Each band of AP has 16 vertically stacked PMTs with a combined field-of-view (FOV) of 22 deg (H) × 3.6 deg (V) [*Chern et al.*, 2003; *Mende et al.*, 2005; *Kuo et al.*, 2005]. The ISUAL Imager, SP and AP are coaligned at the center of their views. ISUAL Imager and SP are bore-sighted, and their FOV is approximately 20 deg (H) × 5 deg (V). Figure 1 shows the observational geometry of the ISUAL payload onboard the FORMOSAT-2. The Imager and SP FOVs project out an area of nearly two million square kilometers on Earth's surface (the gray area in Figure 1), with the near edge at a distance of 2370 km (lateral $\overline{AB} \sim 910$ km), the limb at 3370 km away (lateral $\overline{CD} \sim 1210$ km) and the far edge for 90 km altitude at a distance of 4410 km (lateral $\overline{EF} \sim 1590$ km).

3. Model Formulation

3.1. Electromagnetic FDTD Model

[5] The electromagnetic FDTD model simulates the effects of the electromagnetic pulse (EMP) released by the vertical current of a cloud-to-ground lightning in a circularly symmetric ($\frac{\partial}{\partial\phi} = 0$) cylindrical coordinate system (r, ϕ, z), and involves Maxwell equations that couples with an electron density continuity equation [*Pasko et al.*, 1998; *Veronis et al.*, 1999]. The spatial-and-temporal-varying lightning current waveform is assumed to posses the following form,

$$J_s(r,z,t) = I_p T(t) S(r,z). \tag{1}$$

Here, the peak current I_p occurs at $t = \tau_r$; $T(t)$ is the time-varying function of the current waveform, and $T(t) = \frac{t}{\tau_r}$ at $t < \tau_r$ or $e^{-\left[(t-\tau_r)/\tau_f\right]^2}$ at $t \geq \tau_r$ where τ_r and τ_f are the risetime and the fall-time of the current. The current waveform of the +CGs typically has a risetime of ~10 μs [*Rakov and Uman*, 2003, p. 233], which is longer than that of the −CGs (~5 μs) [*Rakov and Uman*, 2003, p. 7]. The risetimes of the +CG current waveform could be up to hundreds of microseconds for very long upward negative leaders [*Rakov and Uman*, 2003, p. 234]. However, such a complex discharge process is not considered in our modeling. The fall-time of the current waveform is in the order of hundreds of microseconds [*Rakov and Uman*, 2003, p. 215, and references therein]. Therefore for a typical +CG, the risetime τ_r and the fall-time τ_f is chosen to be 10 μs and 100 μs in our model. Figure 2a shows a +CG with a peak current of 280 kA and $\beta = 0.5$, which gave the best fitted to the ISUAL recorded elve on 7 August 2004 1801:22 universal time (UT) and is less than the highest directly measured +CG currents of ~300 kA [*Rakov and Uman*, 2003, p. 214, and references therein]. The spatial distribution function of the current waveform satisfies $S(r,z) = \frac{1}{A_0} e^{-r/r_0^2}$ for $z < a$ or $\frac{1}{A_0} e^{-r/r_0^2-(z-a)^2/z_0^2}$ for $z \geq a$, where A_0 is a normalized area constant and $A_0 = \int_0^\infty e^{-r/r_0^2} 2\pi r dr = \pi r_0^2$; r_o and z_o are chosen to be three times of the cell sizes in the r direction (2 km) and z direction (0.5 km), and a is the current channel length which is assumed to be 10 km. The current channel length is typically 6 km for −CG and 10 km for +CG. The expected disparity between them is in the distance effect, which is less significant for far field (>100 km) since the E field magnitude decays as $E(r) \sim \frac{1}{r}$ at the elves altitude. From our numerical studies, the maximum E fields at elve altitude 87 km were ~30 V/m and ~27 V/m for a current channel length of 10 km and 6 km, respectively. Also, if the current risetime is 5 μs, instead of 10 μs, the E field magnitude from a typical −CG or +CG at the elve altitude would differ by less than 5%. The FDTD model itself is independent of the polarity of the CGs. Also the E field deviation due to the changes in the current waveform and channel length is less than 10%.

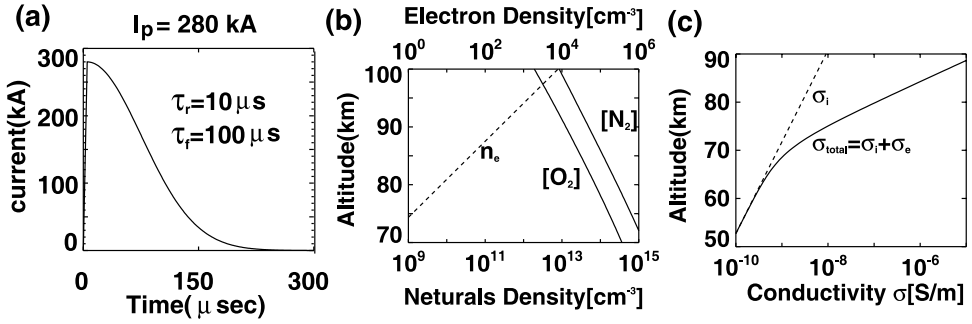

Figure 2. (a) Current waveform (peak current 280 kA, risetime $\tau_r = 10$ μs, and fall-time $\tau_f = 100$ μs) for an assumed CG lightning in our electromagnetic FDTD model, (b) assumed profiles of the neutral species density, electron density in the upper atmosphere, and (c) the total conductivity including both ionic and electronic contributions.

[6] The assumed Gaussian form of the current channel width makes the calculated pulses (E or B field) propagation smoother and reduces the ringing effect due to the numerical dispersion [*Taflove and Hagness*, 2005, p. 34]. The large sampling grid, $3\Delta r$, of the current pulse decreases the error in computing the phase velocity [*Taflove and Hagness*, 2005, Figure 2.2, p. 35]. However, these requirements make the lightning channel unusually broad. For a field point at an altitude of 87 km, the distance between current channel center and the field point is $|\vec{r}| \geq 87$ km. At the far-field limit $|\vec{r}| \gg |\vec{r}'|$, the E field magnitude at field point is proportional to $|\vec{r} - \vec{r}'|^{-1} \approx |\vec{r}|^{-1}\left(1 - \frac{|\vec{r}'|}{|\vec{r}|}\cos\eta\right)$ where the distance between the lightning channel center and broad current channel edge $|\vec{r}'|$ is about 6 km ($3\Delta r$), and η is a angle between $\vec{r}$ and $\vec{r}'$. The expected error owing to the broad current channel is minor since $|\vec{r}| \gg |\vec{r}'|$. This assessment will be further confirmed in section 4.1, by comparing the predicted E field from the FDTD model and that computed by transmission line model (TL) at 100 km away.

[7] We used the MSIS model [*Hedin*, 1991] to calculate molecular nitrogen and molecular oxygen density profiles in our model. The ambient electron density profile is shown in Figure 2b and has the form of $n_e(z) = 1.43 \times 10^7 \exp(-0.15 \times h_0) \exp[(h_\beta - 0.15) \times (z - h_0)]$ (cm^{-3}), where $h_\beta = 0.5$ km^{-1} at the effective reflection height; z is the altitude of interest in units of kilometers and h_0 is the nighttime VLF reflection height of ~85 km [*Cummer et al.*, 1998; *Barrington-Leigh et al.*, 2001]. In Figure 2c, the total conductivity used in our model can be calculated using $\sigma_{total} = \sigma_i + \sigma_e$, which contains both the ion (σ_i) and electron (σ_e) components. The ambient ion conductivity profile is adopted from *Volland*'s [1995] model, $\sigma_i = 1/\sum_{i=1}^{3} A_i e^{-B_i z}$ where $\left(\frac{A_i}{10^{12}\Omega m}, \frac{B_i}{km^{-1}}\right) = (46.9,\ 4.527)_1,\ (22.2,\ 0.375)_2,\ (5.9,\ 0.121)_3$, [*Volland*, 1995, p. 249, and references therein]. The electron conductivity is represented by $\sigma_e = q_e \mu_e N_e$ where q_e is electron charge, N_e is electron density, and μ_e is mobility, which is a function of the reduced E field, E/N, and can be derived from experimental swarm data [*Pasko et al.*, 1997, and references therein]. The electron component σ_e of the total conductivity is a low-frequency approximation (wave frequency, ω, is much lower than the electron collision frequency, ν_{eff}). Arguably, besides depending on the electron density, conductivity is also a function of the wave-frequency via $\sigma(\omega) = \frac{q_e^2 n_e}{m_e \nu_{eff}} \frac{1}{\left(1 + \omega^2/\nu_{eff}^2\right)}$ [*Raizer*, 1997, p. 44] where m_e is electron mass. At 87 km altitude, the collision frequency $\nu_{eff} = \frac{q_e}{m_e \mu_e}$ is 16 MHz for $E = E_k$, which is the conventional breakdown threshold field and will be defined in the text after equation (2), and the collision frequency is 0.6 MHz for a low field $E \approx 0$; the collision frequencies at this altitude for both E fields are much higher than the wave frequency in the VLF range (3–30 kHz). Moreover, electromagnetic pulses with E field strength exceeding 0.3 times of the conventional breakdown threshold field at this altitude is sufficient to induce the first positive band nitrogen emissions of elves [*Veronis et al.*, 1999]. Therefore treating the conductivity as a low-frequency approximation will have minor effect on our emission calculation, thus $\sigma(\omega) \approx \frac{q_e^2 n_e}{m_e \nu_{eff}} = q_e \mu_e n_e$ is used in conductivity term of Maxwell equations. The electron density continuity equation is

$$\frac{dn_e}{dt} = (\nu_i - \nu_a) n_e, \tag{2}$$

where n_e, ν_i and ν_a are the electron density, the ionization rate and dissociative attachment ($O_2 + e^- \rightarrow O^- + O$) rate, respectively. The values of ν_i and ν_a are related to the strength of the E field which will be derived from Maxwell equations. The conventional breakdown threshold field is defined as the E field that produces $\nu_i = \nu_a$ [*Raizer*, 1997, pp. 135–136; *Liu et al.*, 2006]. In return, the change in electron density will modify the ambient conductivity and alter the strength of the E field. The three-body attachment process ($A + O_2 + e^- \rightarrow A + O_2^-$), where A is molecular oxygen or molecular nitrogen in the lower-ionosphere D region, has a timescale >1 s and is not included, since the model deals with processes that last only for a few milliseconds [*Glukhov et al.*, 1992; *Pasko et al.*, 1997].

[8] The numerical simulation domain extends from z = 0 km to z = 100 km and r = 600 km. For EM waves in the VLF range (3–30 kHz), where the lightning radiated

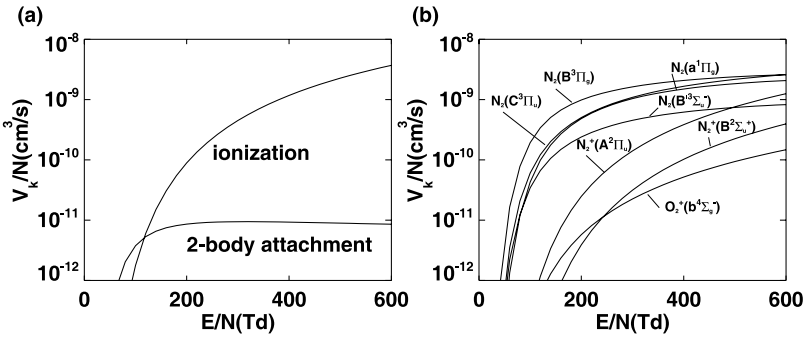

Figure 3. (a) Ionization and two-body attachment rates of oxygen molecules. (b) Optical excitation coefficient for the electronic band systems of molecular nitrogen and molecular oxygen.

electromagnetic field is most intense, the ground and the boundary at 100 km altitude can be assumed to be perfectly conducting [*Inan et al.*, 1996]. For the boundary at 100 km, a previous study has shown that only negligible EM wave energy can penetrate into the lower ionosphere above 95 km altitude [*Taranenko et al.*, 1993]. For a vertical lightning current above a perfectly conductive ground, only the vertical component of the radiated E field is observed at a far-field point on the ground. For an imperfectly conductive ground, the image current below the ground is not strictly equal to the magnitude of lightning current above it. The horizontal component of the E field contributed by the real and the image currents does not cancel. However, in our model, we assume the ground to be perfectly conductive and the tilting effect of lightning current has not been considered [*Rakov and Uman*, 2003, p.162, and references therein].

3.2. Optical Emission Models

[9] We use the ELENDIF code [*Morgan and Penetrante*, 1990] and the cross section data of $N_2(B^3\Pi_g)$, $N_2(C^3\Pi_u)$, $N_2(B'^3\Sigma_u^-)$, $N_2(a^1\Pi_g)$ [*Cartwright et al.*, 1977], $N_2^+(A^2\Sigma_u^+)$ [*Cartwright et al.*, 1975] and $N_2^+(B^2\Sigma_u^+)$ [*Borst and Zipf*, 1970; *Van Zyl and Pendleton*, 1995] to derive the ionization and dissociative attachment rates used in equation (2), which are shown in Figure 3a. Additional cross section data are from the compilation of A. V. Phelps (http://jilawww.colorado.edu/www/research/colldata.html). Figure 3b shows the excitation rates calculated using ELENDIF for the major emission bands of molecular nitrogen and molecular oxygen. Since ELENDIF adopts only a two-term spherical harmonic expansion and is not strictly valid at high E field values. However, recent studies using a Monte Carlo model of thermal runaway electrons produced results that agree with those from the ELENDIF code for electric fields up to $\sim$20 E_k [*Moss et al.*, 2006], which is much higher than the E field of $<$5 E_k generated by the lightning EMP at the altitude of $\sim$90 km.

[10] The number density of the kth excited state at coordinate r, z and time t, $n_k(r, z, t)$, is calculated using the population and depopulation equation [*Sipler and Biondi*, 1972],

$$\frac{\partial n_k}{\partial t} = v_k n_e - n_k\left(A_k + k_{q,N_2}N_{N_2} + k_{q,O_2}N_{O_2}\right) + \sum_m n_m A_m, \quad (3)$$

where v_k, A_k, k_{q,N_2}, k_{q,O_2} are the excitation rate from ELENDIF, the Einstein coefficient, and the collisional quenching rates for the kth electronic state of molecular nitrogen and molecular oxygen as listed in Table 1; n_e, N_{N_2} and N_{O_2} are the number densities of electrons, molecular nitrogen and molecular oxygen. The last term in the right hand side is a sum over all the cascade terms into the specified kth excited state. As an example, for $B^3\Pi_g$, we consider major cascading terms from $C^3\Pi_u$ and $B'^3\Sigma_u^-$ [*Milikh et al.*, 1998] that will be discussed in section 6. The photon emission intensity per volume in units of the number of photons per cubic centimeter per second (ph/cm^3/s) at coordinate r, z and time t for the kth excited state is representing by $I_k(r, z, t) = n_k(r, z, t)A_k$, in the $1PN_2$, $2PN_2$,

Table 1. List of Major Emission Band Systems and Key Parameters of Molecular Nitrogen

Emission Band System	Transition	Wavelength, nm	A_k, s^{-1}	k_{q,N_2}	k_{q,O_2}
$1PN_2$	$N_2(B^3\Pi_g) \rightarrow N_2(A^3\Sigma_u^+)$	478–2531[a]	1.7×10^4 [b]	1.60×10^{-11} [d]	1.50×10^{-10} [d]
$2PN_2$	$N_2(C^3\Pi_u) \rightarrow N_2(B^3\Pi_g)$	268–546[a]	2.0×10^7 [c]	1.12×10^{-11} [e]	2.85×10^{-10} [e]
LBH N_2	$N_2(a^1\Pi_g) \rightarrow N_2(X^1\Sigma_g^+)$	100–260[a]	1.8×10^4 [b]	2.20×10^{-11} [f]	4.30×10^{-10} [f]
Meinel N_2^+	$N_2^+(A^2\Sigma_u^+) \rightarrow N_2^+(X^2\Sigma_g^+)$	550–1770[a]	7.2×10^4 [b]	1.12×10^{-11} [g]	2.9×10^{-10} [g]
$1NN_2^+$	$N_2^+(B^2\Sigma_u^+) \rightarrow N_2^+(X^2\Sigma_g^+)$	286–587[a]	1.6×10^7 [b]	4.53×10^{-10} [e]	7.36×10^{-10} [e]

[a][*Lofthus and Krupenie*, 1977].
[b]On the basis of a private discussion [*Liu and Pasko*, 2005], the middle value of Einstein coefficient (A_k) for major vibrational levels of upper state of band system [*Gilmore et al.*, 1992, Table 19] is used in our model.
[c]The lower Einstein coefficient [*Vallance-Jones*, 1974, p. 119] provides a better fit for our observation and is 74% of that listed by *Gilmore et al.* [1992, Table 19].
[d][*Piper*, 1992].
[e]At this value the quench heights for $2PN_2$ and $1NN_2^+$ are $\sim$30 and $\sim$48 km [*Pancheshnyi et al.*, 1997].
[f]The quench height is $\sim$84 km [*Marinelli et al.*, 1989, Table 1].
[g]The quench height is $\sim$80 km [*Piper et al.*, 1985].

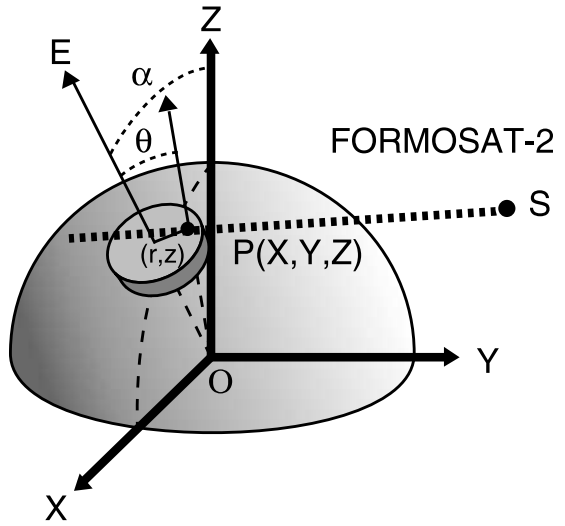

Figure 4. Geometry for modeling ISUAL recorded elves, where the numerical simulating domain of the electromagnetic FDTD model in the 2-D cylindrical coordinate is represented by a disk with a symmetrical axis, $\overline{OE}$ and $\overline{OE}$ makes an angle α with $\overline{OZ}$ (z axis). Simulated reading in each pixel of the ISUAL Imager is an integration of the optical emissions from every point (at time $t' = t - \overline{SP}/c$) along the line-of-sight from satellite to the elve and beyond. More specifically, the emission from Point $P(X, Y, Z)$ can be obtained by converting its coordinates into the circularly symmetric cylindrical coordinates $P(r, z)$ and using electromagnetic FDTD model to compute the emission at this point.

LBH N_2, Meinel N_2^+ and $1NN_2^+$ band systems in our model. The emission lines of the vth vibrational state of the kth excited state into the v'th vibrational state of the k'th excited state is calculated by

$$I_{k,v;k',v'}(\lambda) = n_k q_{x,0;k,v} A_{k,v;k',v'} \tag{4}$$

where λ is the wavelength, and n_k is the number density of the ambient molecular nitrogen or molecular oxygen; $q_{x,0;k,v}$ is the Franck-Condon factor, which represents the relative population of the vth vibrational level of the kth excited state from the 0th vibrational state of the ground state; $A_{k,v;k',v'}$ is the Einstein coefficient from the vth vibrational state of kth electronic state to the v'th vibrational state of k'th electronic state, and the adopted value is from *Gilmore et al.* [1992].

3.3. Observational Geometry for Modeling ISUAL Elves

[11] Figure 4 illustrates the observation geometry for modeling ISUAL recorded elves. The cylinder shape simulation domain in the electromagnetic FDTD model is represented by the column on Earth surface with $\overline{OE}$ as the symmetrical axis. For point $P(X, Y, Z)$ along the line-of-sight from FORMOSAT-2 (indicated by S), its coordinates can also be written as $P(r, z)$ by letting $r = \overline{OP} \cdot \theta$ and $z = \overline{OP} - R_E$ where $\overline{OP} = \sqrt{X^2 + Y^2 + Z^2}$, θ is the angle between $\overline{OE}$ and $\overline{OP}$, and R_E is Earth radius (~6378 km). The reading in the ISUAL Imager pixel is an integration of the optical emissions from all points along the line-of-sight, where the emission intensity emission intensity (ph/cm^3/s) at $P(r, z)$ has to be computed [*Veronis et al.*, 1999; C. P. Barrington-Leigh, private communication, 2006]. Hence one needs to compute the column flux along path L, $S_k(t) = \int_L n_k(X, Y, Z, t - \frac{l}{c}) A_k dl$ (ph/cm^2/s), where $n_k(X, Y, Z, t - \frac{l}{c})$ (cm^{-3}) is the number density of the kth excited state in the Cartesian coordinate (X, Y, Z) at time $t' = t - \frac{l}{c}$, c is light speed, A_k is in the unit of ph/s, and l (cm) is the distance between the satellite and the $P(X, Y, Z)$. As shown in Figure 4, $n_k(X, Y, Z, t - \frac{l}{c})$ at point P is transformed into $n_k(r, z, t')$ and its value can be derived via the electromagnetic FDTD model. The length of the emission ray into a pixel of the Imager CCD is characterized by the tangent height h_t. After accounting for the atmospheric transmittance $T(\lambda, h_t)$ and instrument response $R(\lambda)$, the contribution to the Imager or SP readings from kth excited state of molecular band is given by $M_k(h_t) = \frac{\int \sum_{v,v'} I_{k,v;k',v'}(\lambda) T(\lambda, h_t) R(\lambda) d\lambda}{\int \sum_{v,v'} I_{k,v;k',v'}(\lambda) d\lambda}$, where emission lines, $I_{k,v;k',v'}$ can be obtained in equation (4). The simulated reading at time t in each pixel of the ISUAL Imager is given by $S_k(t)\ M_k(h_t)$. However, to improve simulation efficiency, the simulation domain has to be constrained to the region surrounding an elve. Hence the distance between an elve and the satellite has to be inferred before carrying out the computation.

[12] In Figure 5, points O, S, E, and T represent the Earth center (0, 0, 0), the satellite position, the geometric center of elves, and the tangent point of ray $\overline{SE}$ along line-of-sight between the satellite S and an elve with a center at E. Lines $\overline{SO}$, $\overline{TO}$ and $\overline{EO}$ intercept the Earth great circle $\overline{S'T'E'}$ at points S', T', E'. We characterize the ray $\overline{SE}$ from the specified pixel on the CCD to the geometric center of elves by a tangent height, $\overline{TT'}$ or h_t, which is represented by the number of pixels between the airglow upper boundary and the observed geometric center of elves in Figure 6. Hence the distance between the geometric center of elves and satellite can be calculated using the following numerical integration. For elves occurring in front of the limb, the distance is

$$l_{front}(h_t) = \int_{h_e}^{h_s} \left[1 - (h_t + R_E)^2/(h + R_E)^2\right]^{-1/2} dh. \tag{5a}$$

and for elves appearing behind the limb, the distance is

$$l_{behind}(h_t) = 2\int_{h_t}^{h_e} \left[1 - (h_t + R_E)^2/(h + R_E)^2\right]^{-1/2} dh + \int_{h_e}^{h_s} \left[1 - (h_t + R_E)^2/(h + R_E)^2\right]^{-1/2} dh \tag{5b}$$

where h_t, h_e, h_s and R_E are the tangent height of the central ray, the altitude of elve (~87 km), the altitude of satellite (~891 km) and the Earth radius, and $h = \overline{HO} - R_E$ is the

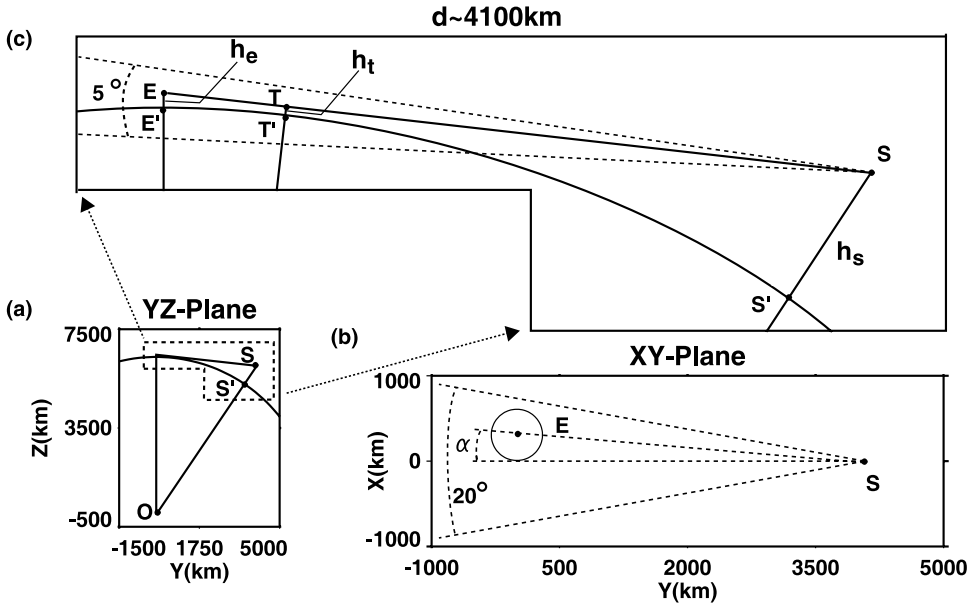

Figure 5. (a) *Y-Z* plane project of Figure 4, (b) *X-Y* plane project of Figure 4, and (c) zoom-in-view of the dashed area in Figure 5a, where Earth center *O*, satellite position *S*, the geometric center *E* of elves, and the tangent point *T* of ray $\overline{SE}$ are labeled, and lines $\overline{SO}$, $\overline{EO}$ and $\overline{TO}$ intercept the Earth's great circle at points S′, E′, T′. Distance and the integrated molecular density of the ray $\overline{SE}$ with the tangent height, $\overline{TT'}$ or h_t can be calculated using equations (5a), (5b), (6a), and (6c). Integrated molecular density can be used to calculate the atmospheric absorption via Lambert's law (also refer to section 3.4).

altitude of a point *H* along the ray $\overline{SE}$. The length of $\overline{HT}$ is $\int_{h_t}^{h} dl_{\overline{HT}} = \int_{h_t}^{h} dh/\sin\theta(h)$, where $\theta(h) = \angle HOT$ and $\sin\theta(h) = [1 - (h_t + R_E)^2/(h + R_E)^2]^{1/2}$. By choosing an appropriate upper limit and lower limit of integration, equation (5) gives the whole length of the ray $\overline{SE}$ [*Mende et al.*, 2005].

3.4. Atmospheric Attenuation

[13] To account for the atmospheric absorption, we considered three major attenuation mechanisms: O_2 absorption, O_3 absorption, and molecular Rayleigh scattering [*Mende et al.*, 2005; *Liu et al.*, 2006]. The ISUAL Imager and SP FOVs are 20 deg (horizontal) × 5 deg (vertical) as shown in Figures 5 and 6. For each ray of emission into the ISUAL Imager and SP with a specified tangent height (h_t), the integrated density for molecular nitrogen, molecular oxygen and ozone along the ray can be represented by the following equations. For in front of the limb emissions, the integrated atmospheric species density in units of cm^{-2} is

$$L_{front}(h_t) = \int_{h_e}^{h_s} N(h)\left[1 - (h_t + R_E)^2/(h + R_E)^2\right]^{-1/2} dh \quad (6a)$$

and for behind the limb emissions, the integrated atmospheric density is

$$L_{behind}(h_t) = 2\int_{h_t}^{h_e} N(h)\left[1 - (h_t + R_E)^2/(h + R_E)^2\right]^{-1/2} dh + \int_{h_e}^{h_s} N(h)\left[1 - (h_t + R_E)^2/(h + R_E)^2\right]^{-1/2} dh \quad (6b)$$

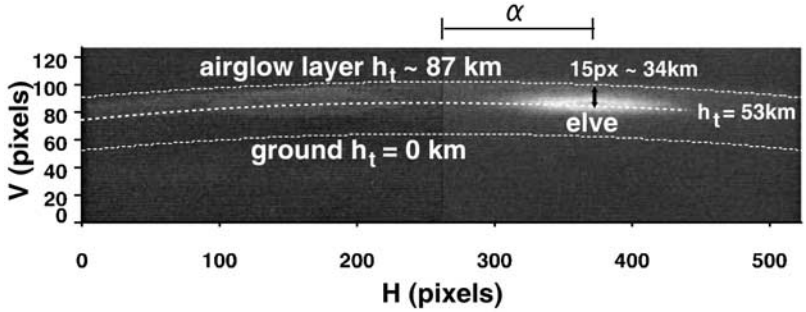

Figure 6. An elve recorded by ISUAL imager on 7 August 2004 1801:22 UT. The angular separation between the geometric center of the elve and the airglow layer is 15 pixels (indicated by the black arrow), which is corresponding to a vertical distance of ~34 km, for an event distance of ~4100 km between the elve (*E*) and the satellite (*S*) in Figure 5a, as indicated by the ray $\overline{SE}$ with a tangent height $h_t \sim 53$ km.

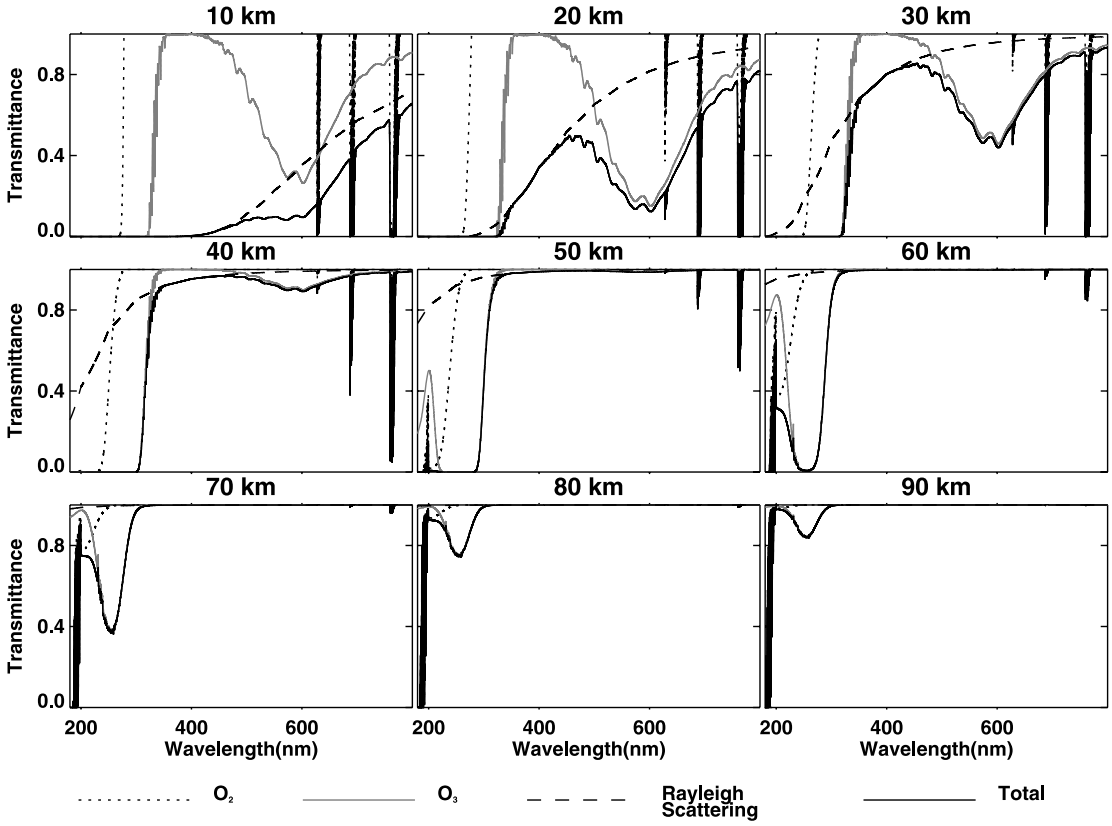

Figure 7. Atmospheric transmittance for the emission wavelength range of 185–800 nm and tangent heights of 10–90 km of behind-the-limb elves. Dashed, gray, long-dashed, and solid lines represent the extinction from O_2, O_3, Rayleigh scattering, and their combined effect.

where h_t is the tangent height of the ray originating from the geometric center of the elve, h_e is the altitude of the elve, h_s is the altitude of satellite and $N(h)$ is the number density of molecular nitrogen, molecular oxygen or ozone as a function of height (h). The nighttime ozone density profile between 18 and 100 km altitude was from the MIPAS measurement (Michelson Interferometer for Passive Atmospheric Sounding) [*Verronen et al.*, 2005]. The ozone density below 100 km accounts for the majority of ozone absorption in our calculated atmospheric extinction. With a known tangent height of the OH airglow (87 km) and a precalibrated vertical angular resolution of the ISUAL Imager, the tangent height h_t for an elves is determined by measuring the angular separation between the airglow layer and the geometric center of elves [*Mende et al.*, 2005].

[14] On the basis of Lambert's law, atmospheric transmittance, $T(\lambda, h_t)$, can be expressed as $T(\lambda, h_t) = \exp(-L(h_t)\sigma(\lambda))$, where $\sigma(\lambda)$ is the absorption cross section in units of cm^2 for the major atmospheric species. The absorption cross sections for molecular oxygen [*Greenblatt et al.*, 1990; *Yoshino et al.*, 1992; *Minschwaner et al.*, 1992; *Amoruso et al.*, 1996; *Yoshino et al.*, 2005], ozone [*Molina and Molina*, 1986; *Burrows et al.*, 1999], and molecular Rayleigh scattering [*Jursa*, 1985, p. 18-8] were compiled and used in computing the atmospheric transmittance. The absorption cross section of molecular nitrogen is very small between 185–800 nm, and its effect on the transmittance is neglected [*Jursa*, 1985, p. 22-4]. Figure 7 shows the atmospheric transmittance in the range of 185–800 nm for behind the limb emissions with different tangent heights. Below 185 nm the transmittance is nearly zero because of absorption of Schumann-Runge continuum and Schumann-Runge bands of molecular oxygen. At tangent height of 87 km, the atmospheric absorption only affects band emissions with wavelength of less than 300 nm. Hence for emission rays originating in front of the limb, we only need to consider the atmospheric absorption on SP1 (LBH band).

3.5. Molecular Band Contributions to ISUAL Imager and SP

[15] An emission ray with a specific tangent height could originate in front of or behind the limb. The atmospheric transmittance depends strongly on the origin of the ray. Figure 8 shows the major molecular nitrogen band contributions to the ISUAL Imager first positive band (1PG) filter and all channels of the ISUAL SP. The responsitivity of the Imager 1PG filter and the ISUAL SP channels are normalized to unity at their central wavelength of the band pass (Imager 1PG filter, 690 nm; SP1, 210 nm; SP2, 337 nm; SP3, 391.4 nm; SP4, 690 nm; SP5, 777.4 nm; SP6, 326 nm). The upper scale of Figure 8 is the distance of elves to satellite. For elves occurring in front of the limb (Figure 8, left), all molecular band contributions, except for SP1, are approximately constant with 26.6% for SP2, 63.2% for SP3, 25.8 for SP4 and 86.6% for SP6. For elves with distance of less than 2500 km (tangent height < 20 km), molecular

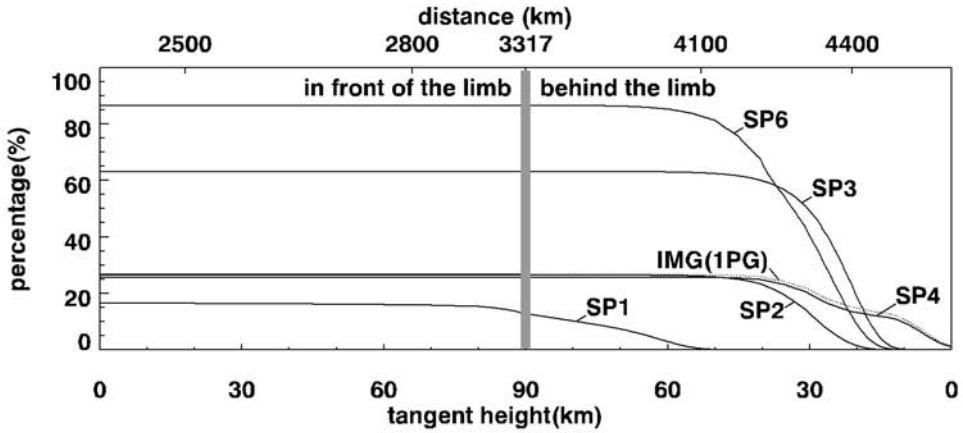

Figure 8. Cumulative molecular band contribution to the ISUAL spectrophotometer channels and Imager (1PG band) for various tangent heights and distances of elves occurring in front of the limb (left) and behind the limb (right).

nitrogen LBH band contribution to SP1 is close to 17%. For elves behind the limb, the molecular nitrogen band contributions to the Imager filter 1 and SP1–SP5 stay nearly constant up to 4100 km, and then decline sharply. SP1 is expected to record no significant molecular nitrogen LBH emission from elves with event distance of greater than 4100 km.

4. Results

[16] Earlier theoretical and numerical studies on the optical emissions of elves have explained the donut-shaped morphology [*Inan et al.*, 1996], predicted the response of photometers and aerial views of the ground cameras [*Veronis et al.*, 1999], and provided a direct comparison with ground-based measurements [*Barrington-Leigh and Inan*, 1999]. Major objectives of this study are to simulate elve emissions as seen from the ISUAL payload onboard the FORMOSAT-2 satellite observation, and to infer the lightning peak currents that generated the observed elve emissions. The present electromagnetic FDTD model, optical emission model and observational geometry and those by *Barrington-Leigh and Inan* [1999] differ in three major ways: Here we (1) explore the 185–800 nm emissions for elves, (2) perform a 3-D geometric mapping by taking the earth curvature into account, and (3) consider the atmospheric absorption of O_2, O_3 and the molecular Rayleigh scattering for the ISUAL satellite observation.

4.1. *EM* Field in Elves

[17] The strength of the B field from a peak current I_p can be derived using the transmission line model (TL) and is given by $B_p = (\upsilon/c)\mu_0 I_p/2\pi d$, where c is the speed of light in vacuum, υ is the propagation speed of return stroke, μ_0 is the magnetic permeability of free space, and d is the distance to CG stroke [*Uman et al.*, 1975; *Orville*, 1987]. The E field is related to the B field by $E = cB$ if the observer is sufficiently far from the lightning. For example, the E field strength on ground and at 100 km away calculated using the TL model with the derived peak NLDN current is known to be well-matched with that recorded by NLDN. The peak current derived from the distant peak E field with $\beta = 0.5$ in TL model also agreed with the directly measured peak current in the triggered rocket experiments within 20–30% [*Cummins et al.*, 1998]. However, in the electromagnetic FDTD model, the propagation speed of the return

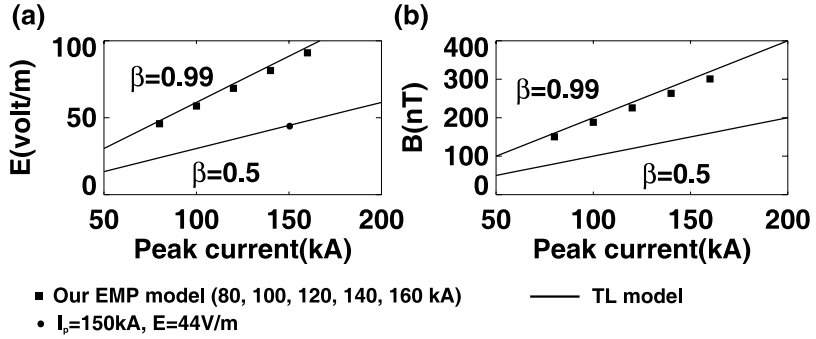

Figure 9. Strength of (a) E field and (b) B field derived using the transmission line (TL) model for various peak currents and at a field distance of 100 km away, where the two lines are for $\beta = 0.5$ and 0.99. Solid squares are E and B fields from the electromagnetic FDTD model at the same distance. β is defined as the ratio between the propagation speed of the return stroke and the speed of light in a vacuum.

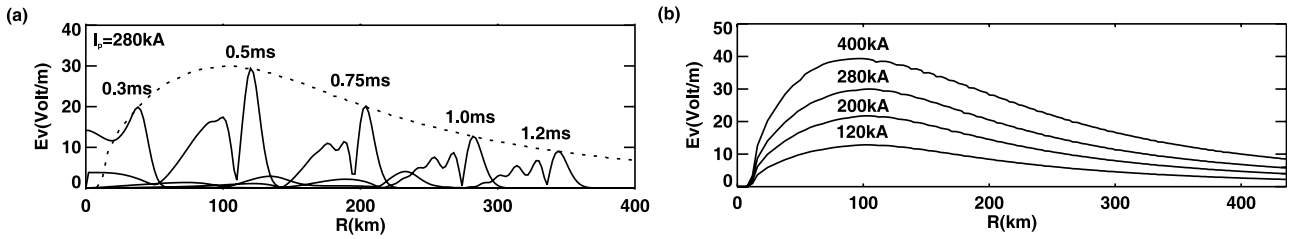

Figure 10. (a) *E* field waveform at the elves altitude of 87 km, at 0.3, 0.5, 0.75, 1.0, and 1.2 ms after a CG peak current of 280 kA at $\beta = 0.5$ and (b) enveloping curves of the maximum *E* fields for modeled elves with peak currents of 120, 200, 280, and 400 kA at $\beta = 0.5$.

stroke has not been factored in explicitly. Hence we need to calibrate the *E* field strength and the causative current in the electromagnetic FDTD model using the TL model. The peak *EM* field at 100 km away from our electromagnetic FDTD model (solid squares) and from TL model (solid lines) are shown in Figure 9, where $\beta = v/c$ is the ratio of the velocity of return stroke to the speed of light in vacuum. The strengths of the *EM* fields in the electromagnetic FDTD model for CG currents of 80, 100, 120, 140, 160 kA are equivalent to those from TL with $\beta = 0.99$. To satisfy the empirical value of 44 V/m on the ground and at a distance of 100 km away as was generated by a peak current of 150 kA [*Inan et al.*, 1996], we found that the choice of a peak current of 75 kA if $\beta = 0.99$ or a peak current of 150 kA if $\beta = 0.5$ in the electromagnetic FDTD model are needed to produce an electric field E_{100} of 44 V/m. To be consistent with the NLDN recorded CG events, we adopt the β value of 0.5 by doubling the values of peak current obtained in our model. It should be noted that, for typical −CGs with β values of 0.33–0.66 and +CGs with $\beta \sim 0.33$, the propagation velocities of the return strokes are $1 - 2 \times 10^8$ m/s [*Rakov and Uman*, 2003, and references therein]. Hence the value of the derived peak current sensitively depends on the choice of the β value in the lightning return stroke.

[18] Figure 10a shows the calculated time-varying waveform of the total magnitude of *E* field E_v, including vertical and radial component of *E* field, at elve altitude (87 km) from a lightning stroke with a peak current of 280 kA if $\beta = 0.5$. The snapshots of *E* waveform are taken at 0.3, 0.5, 0.75, 1.0 and 1.2 ms. At each instance, the *E* field waveform is double-peaked. The first peak originates from the source current in the electromagnetic FDTD model, and the second peak is from the mirror current due to the perfect conductivity boundary at ground in our numerical domain. Owing to its closer range, the first peak has a higher *E* field magnitude and has a dominant effect on heating of electrons at elves altitude. The dashed enveloping curve in Figure 10a shows the radial distribution of the generated *E* field. Figure 10b shows the radial distribution of generated *E* field from several peak currents (120 kA, 200 kA, 280 kA, and 400 kA at $\beta = 0.5$) studied in our model.

4.2. Emissions From Elves

[19] Figure 11 shows a cross-sectional view of the spatial distribution of emissions ($1PN_2$, $2PN_2$, LBH N_2, Meinel N_2^+, $1NN_2^+$) from a modeled elve in the cylindrical coordinate system. The contour lines indicate the time-integrated photon emission number per cubic centimeter (ph/cm^3). In

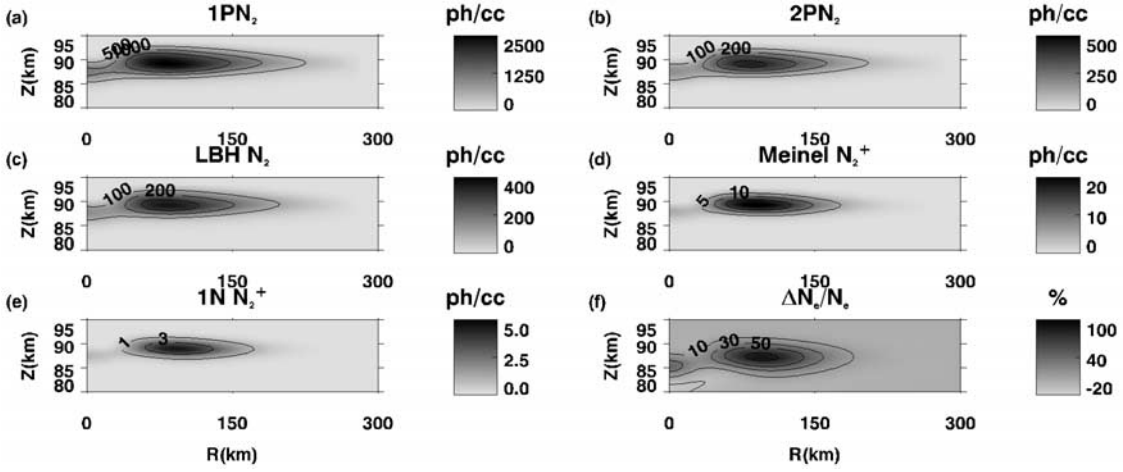

Figure 11. The time-integrated and spatial distribution of emissions from $1PN_2$, $2PN_2$, LBH N_2, Meinel N_2^+, and $1NN_2^+$(a–e) for modeled elves in cylindrical coordinates. Contour lines represent various time-integrated intensities of the produced photons per cubic centimeter (ph/cm^3). (f) Normalized induced electron density change ($\Delta N_e/N_e$).

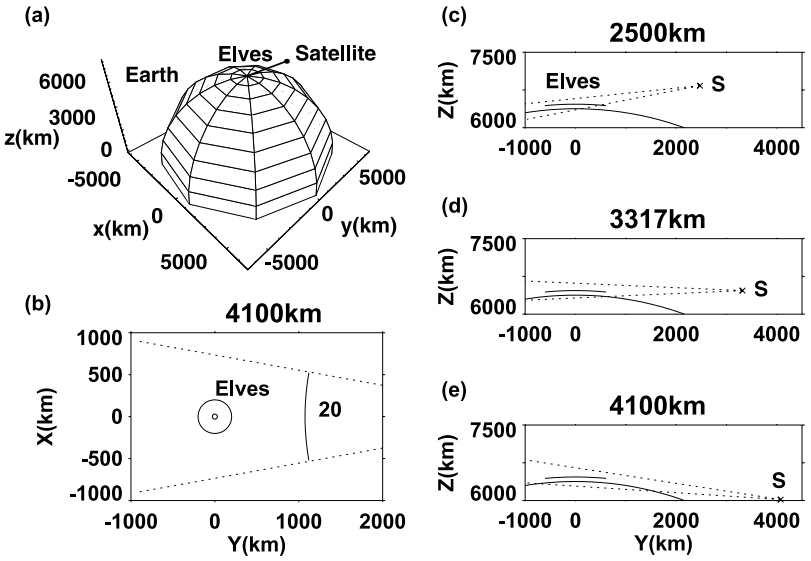

Figure 12. (a) Coordinates (*X*, *Y*, *Z*) of the "central" geometric system. (b) The *X*-*Y* plane projection with the two dashed lines representing the 20-degree lateral FOV of the ISUAL Imager. (c–e) The *Z*-*Y* plane projections of elves, satellite, and FOV for elves occur in front of (Figure 12c), above (Figure 12d), and behind (Figure 12e) the limb. To simply the simulation, the modeled elves are assumed to occur along the *z* axis in the "central" geometric system.

this case, the peak current of the CG lightning is assumed to be 280 kA if $\beta = 0.5$. With the enveloping curve of peaks of the *E* field produced by lightning at altitude 87 km (Figure 10b), the maximum optical emissions and the electron density enhancement occur roughly 90–100 km horizontally away from the lightning at altitude 87 km and with a time delay of ~450 μs after the return stroke. Figure 11f shows that the electron density enhancement can be as high as 70% along a ring-shaped structure of horizontal width ~35 km. The brightness of emission varies greatly depending on the level of the ambient electron density and the peak current of the causative lightning. The most intense optical emissions for the simulated elve in Figure 11 is consistent with that observed by ISUAL imager at the airglow altitude of ~87 km triggered by a parent lightning near the limb, see also Figure 15 (b1).

4.3. Spatial Distribution of Emissions in Elves

[20] To simplify the computation, the satellite in Figure 4 is constrained to move in the *Y*-*Z* plane and the symmetrical axis $\overline{OE}$ is assumed to be the *z* axis, thus the angle α is zero. Therefore the geometric center of modeled elves is horizontally centered at the FOV of the ISUAL Imager (the angle α in Figure 6 also is zero). The coordinates (*X*, *Y*, *Z*) of the geometric center of modeled elves are (0, 0, $R_E + h_e$) where h_e is the elve altitude of ~87 km. The satellite position is stipulated by the distance between the elve and satellite as shown in Figures 12c, 12d, and 12e for top viewing (2500 km), side viewing (3317 km), and bottom viewing (4100 km).

[21] To predict the Imagery of elves in a wide-FOV camera, the time-of-flight of photons from different regions should be considered [*Barrington-Leigh et al.*, 2001]. The predicted spatial-temporal evolution of brightness in elves, in units of mega-Rayleigh (MR), for three event distances of 2500, 3300, and 4100 km is presented in Figure 13. The integration time of each frame is 0.1 ms and the dotted curves in the frame are the tangent height curves of 87 km (top) and 0 km (bottom). The integration time of ISUAL elves images taken through Imager filter 1 (band pass 633–750 nm, for $1PN_2$) was 14 ms and was much longer than the 0.1-ms duration of the frames in Figure 13.

[22] The observational geometry of an elves occurring at a distance of 2500 km away is shown in Figure 12c, in which a space-borne Imager sees the top side of the elve with the near edge located at the lower region of FOV with respect to the far edge. An Imager with sufficient time-resolving power would see a downward curving luminous trace propagating upward since the light from the near edge of ring shape intersection between dipole EMP emission and lower ionosphere arrives before those from the far edge. In the Imager, luminous emissions from an elve occurring in front of the limb would start at the region below the tangent height curve of 0 km, and then propagate upward but never exceeding the 87 km tangent curve. For an elve appearing behind the limb, the Imager will observe the bottom side. In the FOV of Imager, the near edge of the elve is higher than the far edge, but the time-of-flight of the near edge photons is shorter than for those from the far edge. Thus the luminous trace of elves will appear to curve upward and its apparent motion is downward. For elves located right above the Earth's limb, the line-of-sight of Imager is parallel to the luminous plane of elves. The emissions from elves would concentrate on a small area of Imager and no apparent motion of the luminous trace would be detected, except for the trace to lengthen with time. For the ISUAL Imager, the typical integration is 14 ms and is much longer than the frame time in Figure 13. Summing over all the frames for the same event distance in Figure 13 gives the

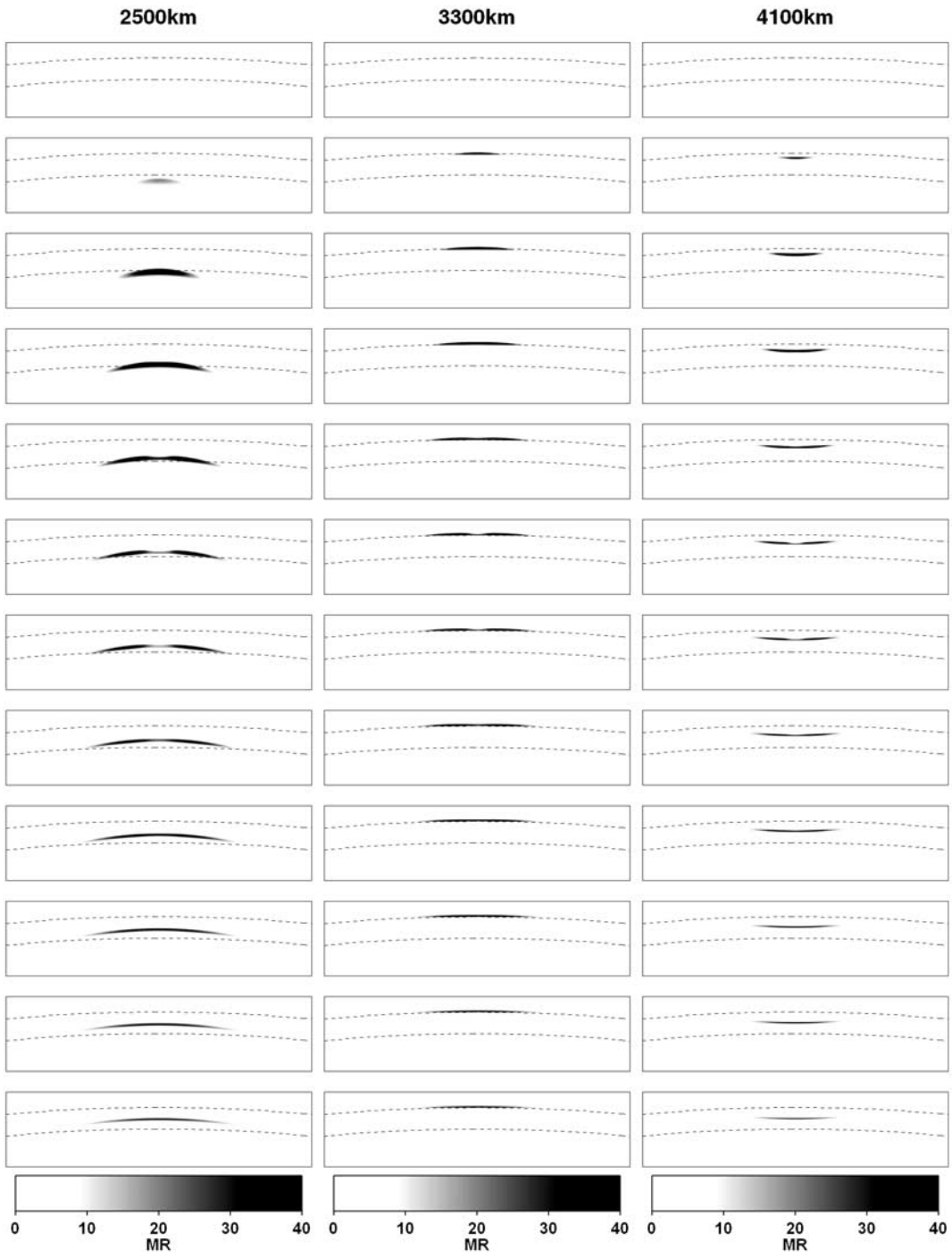

Figure 13. Spatial-temporal evolution of emission $1PN_2$ for a modeled elve from a peak current of 280 kA at $\beta = 0.5$ without considering the atmospheric extinction in units of mega-Rayleigh (MR) at distances of 2500, 3300, and 4100 km away, where the frame integration time is 100 μs. Dashed lines are tangent height curves of 87 km and 0 km, respectively.

composite views in Figure 14, which are the predicted morphologies of elves seen from various distances in the ISUAL Imager.

[23] While ISUAL Imager failed to detect the apparent motion of elves with a 14 ms frame setting, the ISUAL AP does has sufficient vertical spatial (14 km at the limb) and temporal (0.5 ms for the first 20 ms) resolutions to resolve their dynamical evolution. Figure 15 shows three representative ISUAL Imager recorded images, corresponding to elves occurring in front of (a1), at (b1), and behind (c1) the Earth's limb, and red band AP signal traces (a2, b2, and c2) in units of kilo-Rayleigh (kR) at 690 nm, respectively. For elves around the limb, the luminous trace occupies only a single AP channel and no vertical motion is discernible.

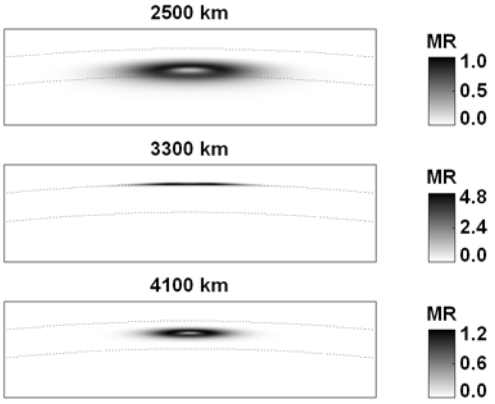

Figure 14. Optical emission $1PN_2$ for a modeled elve (peak current 280 kA at β = 0.5) without considering the atmospheric extinction at distances of 2500, 3300, and 4100 km with a frame integration time of 14 ms. Dashed lines are tangent height curves of 87 km and 0 km, respectively.

Whereas for elves appearing in front and behind the limb, they can straddle multiple AP channels and the apparent vertical motion can be identified.

4.4. Spectrophotometer Readings

[24] Figure 16 illustrates the total column flux (ph/cm^2/s) of emissions ($1PN_2$, $2PN_2$, $1NN_2^+$, LBH, and Meinel band systems) integrated over the SP FOV for elves induced by progressively stronger causative CGs (160 kA to 400 kA at β = 0.5) for event distances of 2500, 3300, and 4100 km, but without considering atmospheric extinction. The important features of time-varying waveforms in Figure 13 include the early sharp rise, the bump at approximately 1 ms and smooth tails. The early sharp peak corresponds to rising region ($\sim$10 μs) of lightning current waveform. The long tail is connected to the expanding shell of radiated *EM* field, whose strength is varying as r^{-1} since the energy of the *EM* field is nearly conserved in the cylindrical coordinate system [*Inan et al.*, 1996]. The bump is most noticeable in the $1NN_2^+$ and Meinel bands since their excitation rates decrease more rapidly at lower *E* field strengths. It should also be noted that the event distance only affects the temporal shape of the total column flux over SP slightly. However, the emission intensities are proportional to r^{-2} and delaying the peak time of the optical emission beyond the lightning onset, referring to the *x* axis in Figure 10a for different radial distances.

[25] The molecular band contribution from elves to various ISUAL photometer channels have been reported in a previous study [*Mende et al.*, 2005], but O_3 attenuation has not been considered, especially for the LBH band, as shown by the gray lines in Figure 7. The atmospheric attenuation for TLEs occurring behinds Earth's limb can be substantial as shown in Figure 8. The predicted photon flux (ph/cm^2/s) that should be measured by SP for elves at distances 2500, 3300, and 4100 km are shown in Figure 17 (left, center, and

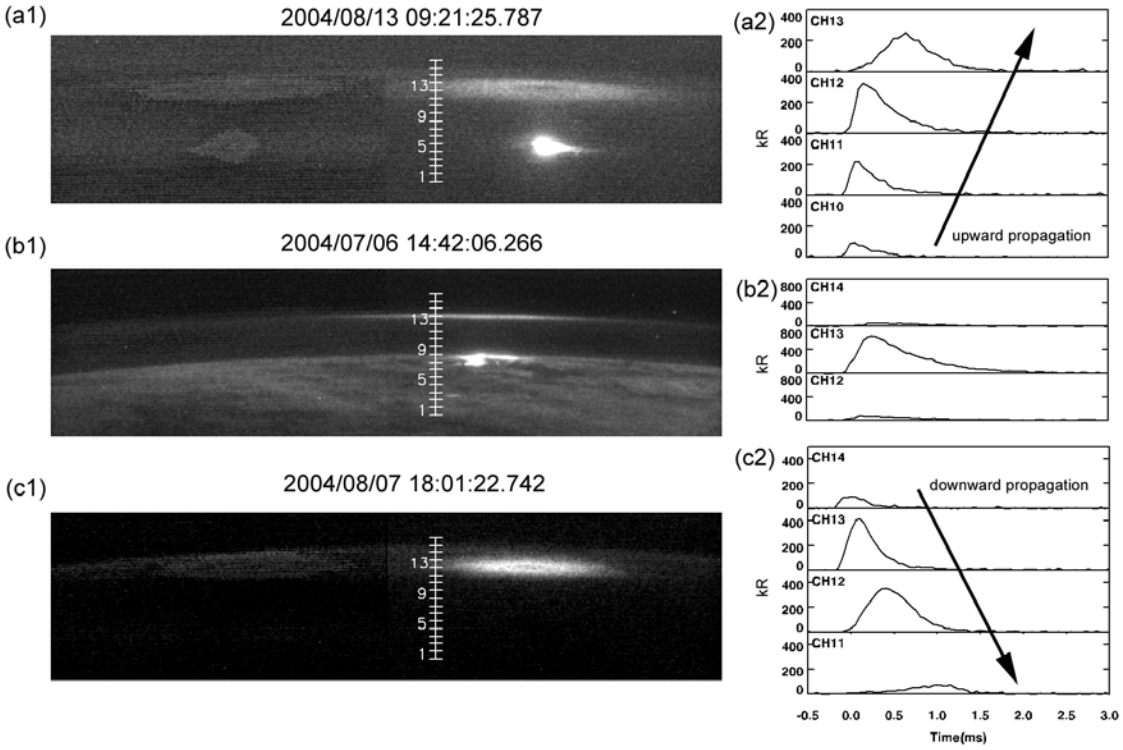

Figure 15. ISUAL Imager (a1, b1, and c1) and AP red band (a2, b2, and c2) data for elves occurring in front, at, and behind the limb. Except for the elves around the limb, the near edge of the elve disk either tilts up (behind the limb) or dips down (in front of the limb) thus resulting in the apparent motion in ISUAL AP.

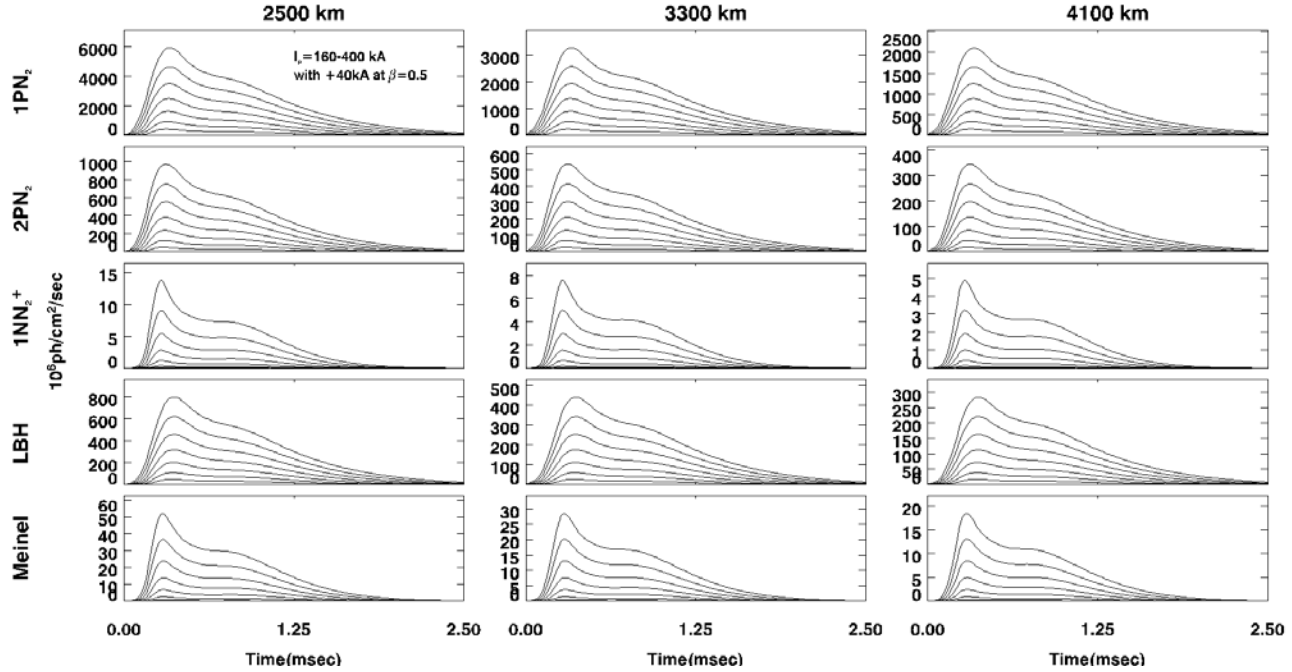

Figure 16. Simulated emission fluxes (top to bottom; $1PN_2$, $2PN_2$, $1NN_2^+$, LBH, and Meinel band systems) from elves in units of photons per square centimeters per second, for elves distances of 2500, 3300, and 4100 km and causative peak currents of 160, 200, 240, 280, 320, 360, and 400 kA at $\beta = 0.5$ without considering the atmospheric extinction.

right). For emissions from elves with tangent heights $h_t <$ 40 km and occurring behind the limb as shown in Figure 8, atmospheric absorption reduces the predicted flux substantially, indicating that the contribution to ISUAL SP1 (LBH band) from the molecular bands depends highly on the tangent height owing to the O_3 attenuation. By comparing the results for elves distance of 2500 km (in front of the limb), 3300 km (above the limb, $h_t \sim 90$ km), and 4100 km (behind

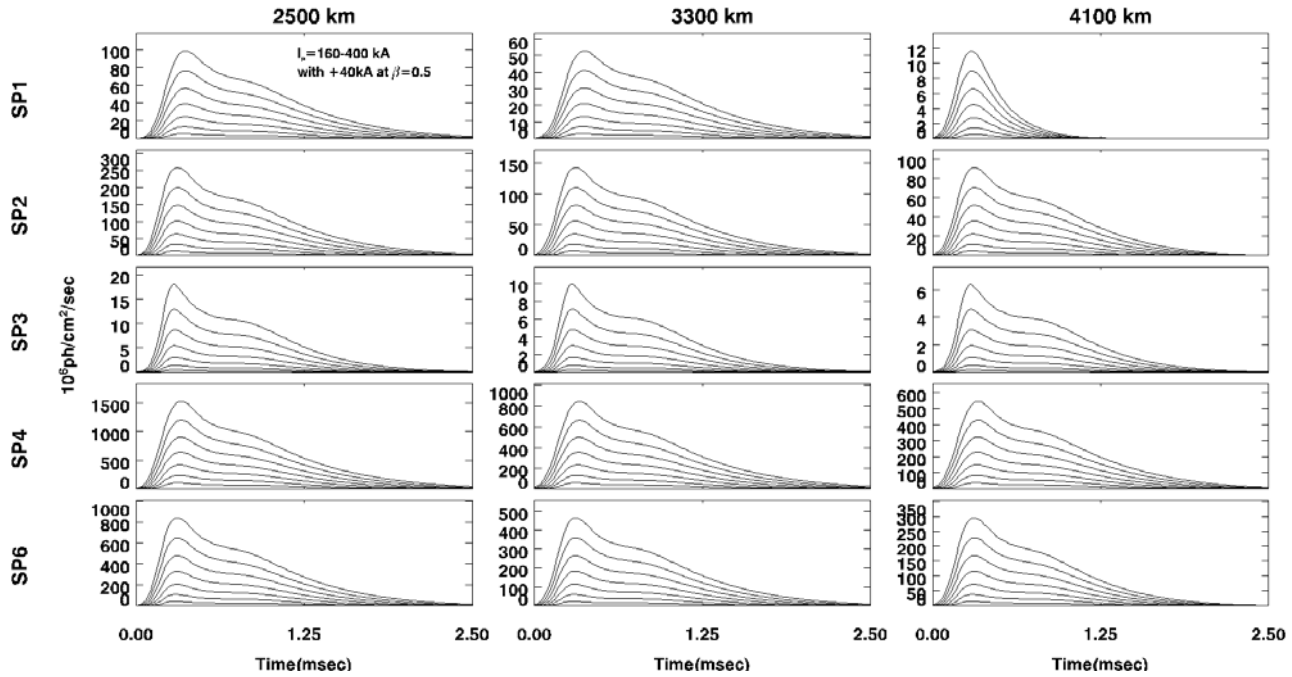

Figure 17. Simulated fluxes of ISUAL spectrophotometer channels with atmospheric extinction for causative CG lightning with peak currents of 160–400 kA at $\beta = 0.5$. For elves behind the limb the reading in SP1 is severely affected by atmospheric absorption.

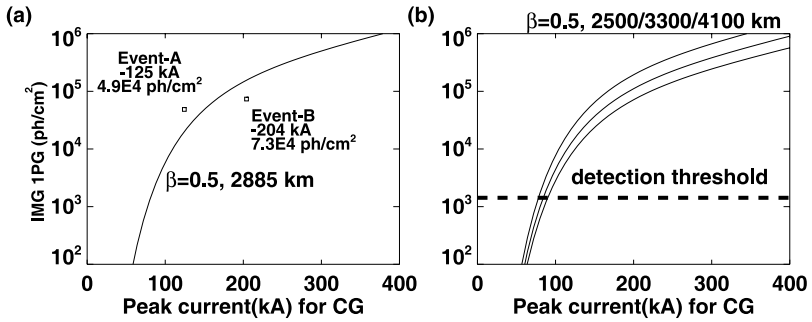

Figure 18. (a) Solid line represents the theoretical time-integrated photon flux observed by ISUAL Imager at a distance of 2885 km as a function of peak current. Also shown are two elves-associated CGs (Events A and B), in which the time-integrated photon fluxes are observed by the ISUAL Imager, and the peak currents are measured by NLDN. (b) Theoretical time-integrated photon fluxes observed by Imager as a function of CG peak currents for elves at distances of 2500, 3300, and 4100 km.

the limb, $30 < h_t < 70$ km), we see that the tail section of predicted SP1 flux is absorbed severely whereas the flux reduction in the other SP channels are not noticeable.

5. Validations of Elves Model

5.1. Validations of Elves Model by Observed CG Peak Current

[26] Five ISUAL recorded elves over the US were found to have possible associated NLDN CGs. However, because of waveform complexity, only two associated NLDN strokes can be geolocated and only one stroke was determined with a high certainty. From the NLDN geolocation information, the separation between these two CG events is reported to be 450 km. VLF magnetic field recordings of the sferics at Duke University show that the two associated strokes (Event A, 28 August 2004 0430:49.547 UT; Event B, 28 August 2004 0430:38.835 UT) occurred at the same azimuth from Duke (estimated from direction finding) and the same range (estimated from signal dispersion), and they were horizontally displaced by less than 100 km from each other. We used these two events to validate the input current of the electromagnetic FDTD model in computing the total time-integrated column flux (ph/cm^2) on Imager optics of elves in the ISUAL Imager (1PG). The two squared-mark data points in Figure 18a are the time-integrated photon flux (ph/cm^2) measured by the Imager from elves induced by these two $-$CGs with NLDN recorded peak currents of -125 kA (Event A; 4.9×10^4 ph/cm^2 with an uncertainty of 15% for ISUAL Imager) and -204 kA (Event B; 7.3×10^4 ph/cm^2 with an uncertainty of 13%).

[27] The solid line in Figure 18a is the total time-integrated column flux on Imager for various strength of peak currents which are compatible with NLDN recorded CG currents; that is, $\beta = 0.5$. On the basis of the time-integrated photon flux measured by SP, the expected peak currents in our model are $\sim$150 and $\sim$170 kA at $\beta = 0.5$ for Event A and Event B. The relative difference between predicted and NLDN peak currents are in close agreement (+25% and -17%, respectively). Interestingly, the peak VLF fields recorded at Duke for these two events are closer than the NLDN peak currents. The Duke magnetic field sensors have a flat response between 100 Hz and 13 kHz, singe pole roll-offs above and below these frequencies, and a sharp 6 pole low-pass cutoff at 25 kHz. The peak VLF magnetic field waveform magnitude was 14.6 nT and 12.0 nT for the lightning strokes associated with Events A and B, respectively. This suggests that the 21.7% difference of peak VLF electric fields at elve altitudes may have been less than the 63% difference as suggested by the NLDN peak currents (-125 kA and -204 kA) and this is more consistent with the 13.3% difference of the inferred peak currents ($\sim$150 and $\sim$170 kA) from the elve optical emissions. The possible reason for the higher difference by NLDN data may be attributed to the unreliable geolocation of the second associated lightning strokes, because both ISUAL and Duke reported that the distance between these two events is less than 100 km. Other uncertainties in this analysis are discussed below in section 6. In Figure 18b, we also plot the simulated total time-integrated column flux (ph/cm^2) as a function of CG peak currents for ISUAL Imager at distances of 2500, 3300, and 4100 km.

5.2. Validation of Elve Model by Emissions Observed From ISUAL Imager

5.2.1. Event 7 August 2004 1801:22 UT

[28] In Figure 19a, ISUAL Imager data of the elve from 7 August 2004 1801:22 UT is overlapped with curves of 87, 53, 30, and 0 km elevations. The dotted lines indicate the region of interest whose brightness distribution was computed and mapped in Figure 19c. The salient properties of this elve, including radius of the elves $\sim$165 km, event distance $\sim$4100 km, apparent brightness $\sim$332 kR for an exposure time 14 ms, and the time-integrated photon flux of $\sim 2.5 \times 10^5$ ph/cm^2 have been deduced and discussed by *Mende et al.* [2005]. To a proper comparison, simulated results of this event with the same exposure time, and the same brightness scale (kR), and in the same geometry system are displayed in Figures 19b and 19d. For this elve, the time-integrated photon flux recorded by Imager was 2.15×10^5 ph/cm^2, while the total time-integrated column flux over Imager for the modeled elves was 1.8×10^5 ph/cm^2. Thus the simulated morphology closely matches the observed, and their photon fluxes are also in good agreement.

[29] The SP waveforms of this elve (solid lines) and the predicted photon fluxes (dotted lines) of a modeled elve with a causative peak current of 264 kA at $\beta = 0.5$ are

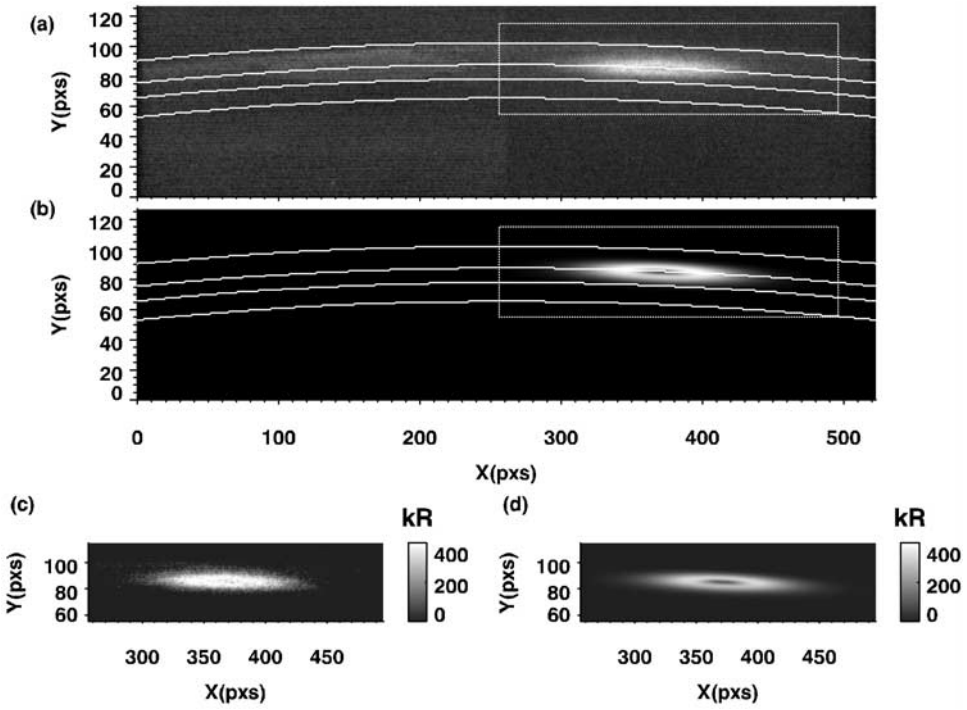

Figure 19. (a) Observed and (b) modeled elves on 7 August 2004 1801:22 UT. Brightness is in units of kilo-Rayleigh (kR). Images are overlapped with tangent height curves of 87, 53, 30, and 0 km. (c and d) Cropped views of the gray dotted rectangles in Figures 19a and 19b.

shown in Figure 20. The observed time-integrated photon fluxes are 1.6×10^3, 2.4×10^4, 1.4×10^3, 1.8×10^5, and 6.2×10^4 ph/cm^2, while the predicted values are 1.7×10^3, 2.5×10^4, 1.2×10^3, 1.7×10^5, and 7.7×10^4 for SP1, 2, 3, 4, and 6. The relative differences are 6%, 4%, 14%, 6% and 23%, respectively. The predicted waveforms of time-varying photon fluxes (ph/cm^2/s) for ISUAL SP match well with those from the observed SP recordings. Some overestimation, especially for SP2 and SP6, occurs at the tail sections of the SP signal traces. For the behind-the-limb elves, the signal in the trailing section originates from the outer edge of the elves, therefore has a smaller tangent height and longer propagation path. Hence the extinction is probably due to aerosol absorption and scattering, which is not included in our calculation of atmospheric attenuation. The major component of the normal upper atmospheric aerosol comes from the time-varying meteoric dust layer, which is difficult to estimate.

5.2.2. Emissions From Elves With Distances From ~3700 to ~4500 km

[30] Table 2 shows the comparative results between the modeled and the observed SP readings of five representative ISUAL elves out of the 105 behind-the-limb elves recorded by ISUAL between August 2004 and November 2005 that have minimal lightning signal mixing in SP readings since their parent lightning was blocked by solid Earth. In order to derive the peak current of the parent lighting from observed elves emissions, we searched for the peak current that produced minimal differences on the time-integrated photon fluxes of SP between the observed and the modeled elves. The difference between modeled and observed fluxes are defined as the *Relative Difference*, $\|I_{mod} - I_{obs}\|/I_{mod} \times 100\%$ where I_{mod} and I_{obs} are the predicted and the observed time-integrated photon fluxes (ph/cm^2) in the ISUAL SP channels. The average relative difference for SP 1 ~ 4 and 6 of 105 ISUAL recorded elves were 44%, 20%, 58%, <1% and 33%, respectively. However, the average relative difference for SP1 (far UV), SP2 (narrow band; 337 nm), SP3 (narrow band; 391.4 nm), and SP6 (mid-UV) were greater, probably owing to the signal in these channels are weaker thus experienced more fluctuation or the unaccounted for aerosol along the emission raypath. Among the 105 behind-the-limb elves analyzed in this work, we found that the

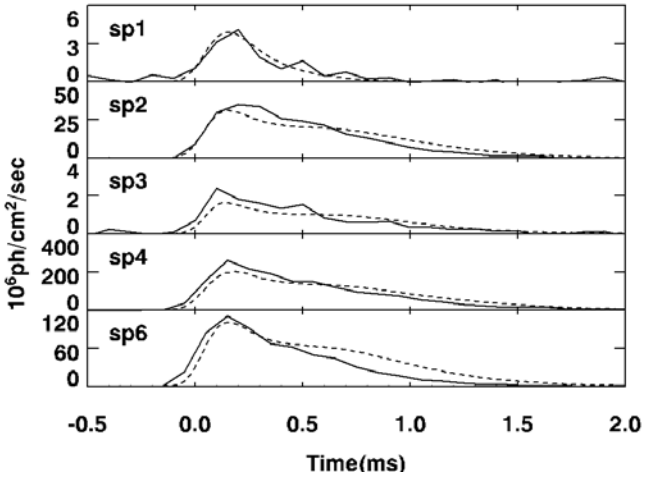

Figure 20. ISUAL spectrophotometer signal traces of the elves on 7 August 2004 1801:22 UT, in which dashed lines are the predicted photon fluxes for a causative lightning with a peak current of 264 kA at $\beta = 0.5$.

Table 2. Comparison of ISUAL SP and Modeled Fluxes for Selected ISUAL Elves

Trigger Time, UT, Distance, km	SP1[a]		SP2[a]		SP3[a]		SP4[a]		SP6[a]		Max. Diff.[b], %	I_p[c], kA
	Obs.[d]	Mod.[d]	Obs.[d]	Mod.[d]	Obs.[d]	Mod.[d]	Obs.[d]	Mod.[d]	Obs.[d]	Mod.[d]		
17 March 2005, 1950:48.725, 3797 km	4.6×10^3	4.9×10^3	2.1×10^4	2.0×10^4	9.5×10^2	9.3×10^2	1.6×10^5	1.5×10^5	5.0×10^4	6.5×10^4	−23	240
21 August 2005, 1126:20.852, 3850 km	2.5×10^3	3.1×10^3	1.5×10^4	1.1×10^4	7.2×10^2	6.6×10^2	1.1×10^5	1.1×10^5	3.9×10^4	4.6×10^4	−15	216
13 September 2005, 1637:45.509, 4080 km	1.1×10^3	1.0×10^3	1.2×10^4	1.3×10^4	6.1×10^2	6.1×10^2	1.0×10^5	1.0×10^5	3.1×10^4	4.1×10^4	−24	220
7 August 2004, 1801:22.742, 4081 km	1.6×10^3	1.7×10^3	2.4×10^4	2.5×10^4	1.4×10^3	1.2×10^3	1.8×10^5	1.7×10^5	6.2×10^4	7.7×10^4	−19	264
11 March 2005, 1442:09.139, 4300 km	N/A	N/A	3.6×10^3	4.6×10^3	3.8×10^2	3.0×10^2	4.7×10^4	4.6×10^4	9.7×10^3	1.4×10^4	−30	250

[a]Measured time-integrated photon flux of ISUAL SP1 ~4 and 6 is in units of ph/cm^2.
[b]Max. Diff. is the maximum relative difference between the predicted and the observed fluxes for SP1 ~4 and 6 in units of %.
[c]I_p is the peak current in the elves model at $\beta = 0.5$, in units of kilo-ampere (kA).
[d]Obs. and Mod. indicate the observed and the modeled time-integrated photon fluxes in ISUAL SP1 ~4 and 6.

causative CG currents were between 160 kA and 400 kA if $\beta = 0.5$. For NLDN data, *Lyons et al.* [1998] reported that the largest recorded −CG peak current was 957 kA, while the largest +CG peak current was 580 kA. However, the deduction of the NLDN current by *Lyons et al.* was based on an empirical formula, similar to our choice of $\beta = 0.5$ in TL model as mentioned above. Their empirical fit assumed that the peak radiated field is linear proportional to the lightning peak current recorded on ground and the return stroke velocities are all the same and are a constant [*Cummins et al.*, 1998]. It should be noted that, in the triggered rocket experiments, no −CG peak current greater than 60 kA was measured and no +CG current was ever recorded [*Orville*, 1999].

6. Discussion

[31] For the major cascading terms in the optical emission model, equation (3), we only consider two upper states ($C^3\Pi_u$ and $B'^3\Sigma_u^-$) of $B^3\Pi_g$ in the $1PN_2$ band. The other possible cascade pathways from $D^3\Sigma_u^+$ can be neglected; because the excitation rate of $D^3\Sigma_u^+$ is about 1 order of magnitude lower than that of $B'^3\Sigma_u^-$ [*Milikh et al.*, 1998, Figure 2]. Using the electromagnetic FDTD model, a CG lightning with a peak current of 280 kA and $\beta = 0.5$ will generate an E field of ~30 V/m (0.45 ms after the CG) at the location of z = 87 km and r = 102 km, which is equivalent to ~300 Td (1 Townsend = 10^{-17} volt cm^2) at 87 km altitude where the nitrogen density is $\sim 10^{14}$ cm^{-3}. The direct excitation rate of $B^3\Pi_g$ at 300 Td (see Figure 3b) is $\frac{\nu_k}{N} \sim 1.6 \times 10^{-9}$ cm^3/s. The direct electron impact excitation, the first term in right hand side of equation (3), is $\nu_k n_e \sim 1.9 \times 10^7$ cm^{-3}/s; whereas the cascading contributions from $C^3\Pi_u$ and $B'^3\Sigma_u^-$ are $n_k A_k \sim 8.2 \times 10^6$ and 9.4×10^5 cm^{-3}/s. The contribution from $B'^3\Sigma_u^-$ was about 11% of that from $C^3\Pi_u$ in our numerical study.

[32] The correlation between the peak emission of elves and the NLDN peak current was first confirmed in ground-based observation, but strictly only for $1PN_2$ band (650–850 nm) [see *Barrington-Leigh and Inan*, 1999, Figure 3b]. For ISUAL data, spectroscopic measurements between 185–800 nm can be used to validate the optical emission model, to elucidate the photometric signatures and to evaluate their correlation with causative CG current, all with a minimal atmospheric extinction. The time-integrated photon flux through ISUAL Imager 1 filter and channels of ISUAL SP are all found to have a correlation with the causative lightning current similar to that in Figure 18. The predicted and the observed photometric fluxes differ by less than 25% (section 5.2.1). One of the causes that may contribute to the difference could be atmospheric aerosols, which are not accounted for in the elves model. Major discrepancy contributors are the ambient electron density profile in the upper atmosphere and the current waveform of the lightning return stroke. The electron density profile used in the elves model is based on the work of *Wait and Spies* [1964], which has a nighttime VLF reflection of 85 km. It is possible that the VLF reflection height could vary from location to location. Taking a modeled elves with peak current 280 kA at $\beta = 0.5$ as an example, if the reflection height is at 88 km, the optical emission intensity of $1PN_2$ would be 5% higher than that with a reflection height of 85 km. If the reflection height further lowers to 83 km or 80 km, the optical intensity of $1PN_2$ will reduce to 58% or 23% of that for h_o is 85 km. To achieve the same effect on the emission intensity, the strength of causative lighting current would needs to be reduced by 20 kA and 50 kA, respectively. Hence the variation of VLF reflection height from the assumed h_o of 85 km could be a major contribution source for the difference between the observed and simulated emission intensity.

[33] The ISUAL Imager provides the most reliable way to identify elves, while the SP readings of elves are always contaminated by lightning emissions and AP cannot resolve the horizontal spatial morphology of elves. The typical brightness of the airglow emission is about 10 kR. To reliably distinguish elves from the airglow background, the brightness of elves should be greater than 30 kR (if S/N = 3). The luminous volume of elves is at least 200 km in width and 2 km in height at the airglow altitude, which will

result in a 100-pixel image in the ISUAL imager (1 pixel ~ 2 km near the limb). Because of the effect of emission integration along the line-of-sight, elve occurring above the limb was the most often observed elves. The extended solid angle per imaging pixel is 4.8×10^{-7} radian and the integrated time is 14 ms for the ISUAL imager in performing these elve observations. By converting the brightness kR into time-integrated photon flux [*Mende et al.*, 2005], the time-integrated photon flux is 1.6×10^3 ph/cm^2, corresponding to the photon flux expected to be generated by an 80 kA CG lightning with $\beta = 0.5$, as shown in Figure 18b. The minimum peak current of the causative CGs for ISUAL recorded elves is 80 kA at $\beta = 0.5$ for NLDN CGs in this study, due to the detection threshold setting of the ISUAL SP and greater elves distances (>2200 km for ISUAL) than those in ground observations (<700 km). The threshold of peak currents for CGs to initiate elves, which was first discussed by *Barrington-Leigh and Inan* [1999], is 60 kA for NLDN recorded causative CGs. *Rakov and Tuni* [2003] estimated that return stroke currents of 151 and 82 kA at $\beta = 0.3$ and 0.5 are needed to initiate elves, on the basis of the TL model. Hence ISUAL did not resolve the threshold peak CG currents for generating elves. However, ISUAL does provide the global occurrence of elves induced by intense lightning current of greater than 80 kA.

7. Summary

[34] We have successfully used the electromagnetic finite difference time domain (FDTD) model to simulate the emissions of elves between 185–800 nm and their spatial-temporal evolution, as seen by a space-borne instrument. Two associated NLDN CG events were found for the analyzed ISUAL elve events, and were used to validate the electromagnetic FDTD model. The derived current based on the ISUAL Imager data for these two elves were found to agree within 25% with those of the associated CG events reported by NLDN. For the ISUAL elves studied in this article, the inferred peak currents of the causative CGs are 160–400 kA if $\beta = 0.5$. The relatively high elves initiation current was due to the high preset triggering level of the ISUAL SP and the long event distances of greater than 3700 km. Therefore ISUAL can be viewed as a space probe of elves induced by intense lightning events.

[35] **Acknowledgments.** Thanks to Victor Pasko and Ningyu Liu for fruitful discussions and to Christopher Barrington-Leigh for comments and support of his optical mapping algorithm. Work performed at NCKU was supported in part by the National Space Center and National Science Council in Taiwan under grant numbers 94-NSPO(B)-ISUAL-FA09-01, NSC95-2112-M-006-016, and NSC95-2111-M-006-002-MY2.

[36] Zuyin Pu thanks the reviewers for their assistance in evaluating this paper.

References

Amoruso, A., L. Crescentini, M. Cola, and G. Fiocco (1996), Oxygen absorption cross-section in the Herzberg continuum, *J. Quant. Spectrosc. Radiat. Transfer*, *56*, 145–152.

Barrington-Leigh, C. P., and U. S. Inan (1999), Elves triggered by positive and negative lightning discharges, *Geophys. Res. Lett.*, *26*, 683–686.

Barrington-Leigh, C. P., U. S. Inan, and M. Stanley (2001), Identification of sprites and elves with intensified video and broadband array photometry, *J. Geophys. Res.*, *106*, 1741–1750.

Boeck, W. L., O. H. Vaughan Jr., R. Blakeslee, B. Vonnegut, and M. Brook (1992), Lightning induced brightening in the airglow layer, *Geophys. Res. Lett.*, *19*, 99–102.

Borst, W. L., and E. C. Zipf (1970), Cross section for electron-impact excitation of the (0, 0) first negative band of N_2^+ from threshold to 3 keV, *Phys. Rev. A*, *1*, 834–840.

Burrows, J. P., A. Richter, A. Dehn, B. Deters, S. Himmelmann, S. Voigt, and J. Orphal (1999), Atmospheric remote-sensing reference data from GOME-2: Temperature-dependent absorption cross sections of O_3 in the 231–794 nm range, *J. Quant. Spectrosc. Radiat. Transfer*, *61*, 509–517.

Cartwright, D. C., W. R. Pendleton Jr., and L. D. Weaver (1975), Auroral emission of the N_2^+ Meinel bands, *J. Geophys. Res.*, *80*, 651–654.

Cartwright, D. C., S. Trajmar, A. Chutjian, and W. Williams (1977), Electron impact excitation of the electronic states of N_2: II. Integral cross sections at incident energies from 10 to 50 eV, *Phys. Rev. A*, *16*, 1041–1051.

Chern, J. L., R. R. Hsu, H. T. Su, S. B. Mende, H. Fukunishi, Y. Takahashi, and L. C. Lee (2003), Global survey of upper atmospheric transient luminous events on the ROCSAT-2 satellite, *J. Atmos. Sol. Terr. Phys.*, *65*, 647–659.

Cummer, S. A., U. S. Inan, and T. F. Bell (1998), Ionospheric D region remote sensing using VLF radio atmospherics, *Radio Sci.*, *33*, 1781–1792.

Cummins, K. L., E. P. Krider, and M. D. Malone (1998), The US National Lightning Detection Network™ and applications of cloud-to-ground lightning data by electric power utilities, *IEEE Trans. Electromagn. Compat.*, *40*(4), 465–480.

Fernsler, R. F., and H. L. Rowland (1996), Models of lightning-produced sprites and elves, *J. Geophys. Res.*, *101*, 29,653–29,662.

Franz, R. C., R. J. Nemzek, and J. R. Winckler (1990), Television image of a large upward electrical discharge above a thunderstorm system, *Science*, *249*, 48–51.

Fukunishi, H., Y. Takahashi, M. Kubota, K. Sakanoi, U. S. Inan, and W. A. Lyons (1996), Elves: Lightning-induced transient luminous events in the lower ionosphere, *Geophys. Res. Lett.*, *23*, 2157–2160.

Gilmore, F. R., R. R. Laher, and P. J. Espy (1992), Franck-Condon factors, r-centroids, electronic transition moments, and Einstein coefficients for many nitrogen and oxygen band systems, *J. Phys. Chem. Ref. Data*, *21*, 1005–1107.

Glukhov, V. S., V. P. Pasko, and U. S. Inan (1992), Relaxation of transient lower ionospheric disturbances caused by lightning-whistler-induced electron precipitation bursts, *J. Geophys. Res.*, *97*, 16,971–16,979.

Greenblatt, G. D., J. J. Orlando, J. B. Burkholder, and A. R. Ravishankara (1990), Absorption measurements of oxygen between 330 and 1140 nm, *J. Geophys. Res.*, *95*, 18,577–18,582.

Hedin, A. E. (1991), Extension of the MSIS thermosphere model into the middle and lower atmosphere, *J. Geophys. Res.*, *96*, 1159–1172.

Inan, U. S., T. F. Bell, and J. V. Rodriguez (1991), Heating and ionization of the lower ionosphere by lightning, *Geophys. Res. Lett.*, *18*, 705–708.

Inan, U. S., W. A. Sampson, and Y. N. Taranenko (1996), Space-time structure of optical flashes and ionization changes produced by lighting-EMP, *Geophys. Res. Lett.*, *23*, 133–136.

Inan, U. S., C. Barrington-Leigh, S. Hansen, V. S. Glukhov, T. F. Bell, and R. Rairden (1997), Rapid lateral expansion of optical luminosity in lightning-induced ionospheric flashes referred to as 'elves', *Geophys. Res. Lett.*, *24*, 583–586.

Jursa, A. S. (1985), *Handbook of Geophysics and the Space Environment*, 4th ed., Air Force Geophys. Lab., Hanscom AFB, Mass.

Kuo, C.-L., R. R. Hsu, A. B. Chen, H. T. Su, L. C. Lee, S. B. Mende, H. U. Frey, H. Fukunishi, and Y. Takahashi (2005), Electric fields and electron energies inferred from the ISUAL recorded sprites, *Geophys. Res. Lett.*, *32*, L19103, doi:10.1029/2005GL023389.

Liu, N., and V. P. Pasko (2005), Molecular nitrogen LBH band system far-UV emissions of sprite streamers, *Geophys. Res. Lett.*, *32*, L05104, doi:10.1029/2004GL022001.

Liu, N., et al. (2006), Comparison of results from sprite streamer modeling with spectrophotometric measurements by ISUAL instrument on FORMOSAT-2 satellite, *Geophys. Res. Lett.*, *33*, L01101, doi:10.1029/2005GL024243.

Lofthus, A., and P. H. Krupenie (1977), The spectrum of molecular nitrogen, *J. Phys. Chem. Ref. Data*, *6*, 113–307.

Lyons, W. A., M. Uliasz, and T. E. Nelson (1998), Large peak current cloud-to-ground lightning flashes during the summer months in the contiguous United States, *Mon. Weather Rev.*, *126*(8), 2217–2233.

Marinelli, W. J., W. J. Kessler, B. D. Green, and W. A. M. Blumberg (1989), Quenching of $N_2(a^1\Pi_g, v' = 0)$ by N_2, O_2, CO, CO_2, CH_4, H_2, and Ar, *J. Chem. Phys.*, *90*, 2167–2173.

Mende, S. B., H. U. Frey, R. R. Hsu, H. T. Su, A. B. Chen, L. C. Lee, D. D. Sentman, Y. Takahashi, and H. Fukunishi (2005), D region ionization by lightning-induced electromagnetic pulses, *J. Geophys. Res.*, *110*, A11312, doi:10.1029/2005JA011064.

Milikh, G., J. A. Valdivia, and K. Papadopoulos (1998), Spectrum of red sprites, *J. Atmos. Sol. Terr. Phys.*, *60*, 907–915.

Minschwaner, K., G. P. Anderson, L. A. Hall, and K. Yoshino (1992), Polynomial coefficients for calculating O_2 Schumann-Runge cross sections at 0.5 cm^{-1} resolution, *J. Geophys. Res.*, *97*, 10,103–10,108.

Molina, L. T., and M. J. Molina (1986), Absolute absorption cross sections of ozone in the 185- to 350-nm wavelength range, *J. Geophys. Res.*, *91*, 14,501–14,508.

Morgan, W. L., and B. M. Penetrante (1990), ELENDIF: A time-dependent Boltzmann solver for partially ionized plasmas, *Comput. Phys. Commun.*, *58*, 127–152.

Moss, G. D., V. P. Pasko, N. Liu, and G. Veronis (2006), Monte Carlo model for analysis of thermal runaway electrons in streamer tips in transient luminous events and streamer zones of lightning leaders, *J. Geophys. Res.*, *111*, A02307, doi:10.1029/2005JA011350.

Orville, R. E. (1987), An analytical solution to obtain the optimum source location using multiple direction finders on a spherical surface, *J. Geophys. Res.*, *92*, 10,877–10,886.

Orville, R. E. (1999), Comments on "Large peak current cloud-to-ground lightning flashes during the summer months in the contiguous United States", *Mon. Weather Rev.*, *127*(8), 1937–1938.

Pancheshnyi, S. V., S. M. Starikovskaya, and A. Y. Starikovskii (1997), Measurements of the rates of quenching of $N_2(C^3\Pi_u)$ and $N_2^+(B^2\Sigma_u^+)$ states by N_2, O_2, and CO molecules in the afterglow plasma of a nanosecond discharge, *Plasma Phys. Rep.*, *23*, 616–620.

Pasko, V. P., U. S. Inan, T. F. Bell, and Y. N. Taranenko (1997), Sprites produced by quasi-electrostatic heating and ionization in the lower ionosphere, *J. Geophys. Res.*, *102*, 4529–4562.

Pasko, V. P., U. S. Inan, T. F. Bell, and S. C. Reising (1998), Mechanism of ELF radiation from sprites, *Geophys. Res. Lett.*, *25*, 3493–3496.

Pasko, V. P., M. A. Stanley, J. D. Mathews, U. S. Inan, and T. G. Wood (2002), Electrical discharge from a thundercloud top to the lower ionosphere, *Nature*, *416*, 152–154.

Piper, L. G. (1992), Energy transfer studies on $N_2(X^1\Sigma_g^+, v)$ and $N_2(B^3\Pi_g)$, *J. Chem. Phys.*, *97*, 270–275.

Piper, L. G., B. D. Green, W. A. M. Blumberg, and S. J. Wolnik (1985), N_2^+ Meinel band quenching, *J. Chem. Phys.*, *82*, 3139–3145.

Raizer, Y. P. (1997), *Gas Discharge Physics*, pp. 135–136, Springer, New York.

Rakov, V. A., and W. G. Tuni (2003), Lightning electric field intensity at high altitudes: Inferences for production of elves, *J. Geophys. Res.*, *108*(D20), 4639, doi:10.1029/2003JD003618.

Rakov, V. A., and M. A. Uman (2003), *Lightning: Physics and Effects*, Cambridge Univ. Press, Cambridge, UK.

Sentman, D. D., E. M. Wescott, D. L. Osborne, D. L. Hampton, and M. J. Heavner (1995), Preliminary results from the Sprites94 aircraft campaign: 1. Red sprites, *Geophys. Res. Lett.*, *22*, 1205–1208.

Sipler, D. P., and M. A. Biondi (1972), Measurements of $O(^1D)$ quenching rates in the F region, *J. Geophys. Res.*, *77*, 6202–6212.

Su, H.-T., R.-R. Hsu, A. B.-C. Chen, Y.-J. Lee, and L.-C. Lee (2002), Observation of sprites over the Asian continent and over oceans around Taiwan, *Geophys. Res. Lett.*, *29*(4), 1044, doi:10.1029/2001GL013737.

Su, H. T., R. R. Hsu, A. B. Chen, Y. C. Wang, W. S. Hsiao, W. C. Lai, L. C. Lee, M. Sato, and H. Fukunishi (2003), Gigantic jets between a thundercloud and the ionosphere, *Nature*, *423*, 974–976.

Taflove, A., and S. C. Hagness (2005), *Computational Electrodynamics: The Finite-Difference Time-Domain Method*, 3rd ed., Artech House, Boston.

Taranenko, Y. N., U. S. Inan, and T. F. Bell (1993), Interaction with the lower ionosphere of electromagnetic pulses from lightning: Heating, attachment, and ionization, *Geophys. Res. Lett.*, *20*, 1539–1542.

Uman, M. A., R. D. Brantley, Y. T. Lin, J. A. Tiller, E. P. Krider, and D. K. McLain (1975), Correlated electric and magnetic fields from lightning return strokes, *J. Geophys. Res.*, *80*, 373–376.

Vallance-Jones, A. (1974), *Aurora*, D. Reidel Publ., Dordrecht.

Van Zyl, B., and W. Pendleton Jr. (1995), $N_2^+(X)$, $N_2^+(A)$, and $N_2^+(B)$ production in $e^- + N_2$ collisions, *J. Geophys. Res.*, *100*, 23,755–23,762.

Veronis, G., V. P. Pasko, and U. S. Inan (1999), Characteristics of mesospheric optical emissions produced by lighting discharges, *J. Geophys. Res.*, *104*, 12,645–12,656.

Verronen, P. T., et al. (2005), A comparison of night-time GOMOS and MIPAS ozone profiles in the stratosphere and mesosphere, *Adv. Space Res.*, *36*, 958–966.

Volland, H. (1995), *Handbook of Atmospheric Electrodynamics*, CRC Press, Boca Raton, Fla.

Wait, J. R., and K. P. Spies (1964), Characteristics of the Earth-ionosphere waveguide for VLF radio waves, *Tech. Note 300*, Natl. Bur. of Stand., Boulder, Colo.

Wescott, E. M., D. Sentman, D. Osborne, D. Hampton, and M. Heavner (1995), Preliminary results from the Sprites94 aircraft campaign: 2. Blue jets, *Geophys. Res. Lett.*, *22*, 1209–1212.

Yoshino, K., J. R. Esmond, A. S. C. Cheung, D. E. Freeman, and W. H. Parkinson (1992), High resolution absorption cross sections in the transmission window region of the Schumann-Runge bands and Herzberg continuum of O_2, *Planet. Space Sci.*, *40*, 185–192.

Yoshino, K., W. H. Parkinson, K. Ito, and T. Matsui (2005), Absolute absorption cross-section measurements of Schumann Runge continuum of O_2 at 90 and 295 K, *J. Mol. Spectrosc.*, *229*, 238–243.

A. B. Chen, R. K. Chou, R. R. Hsu, C.-L. Kuo, Y. J. Lee, H. T. Su, and L. Y. Tsai, Department of Physics, National Cheng Kung University, 1, University Road, Tainan City 701, Taiwan. (johnny@phys.ncku.edu.tw)

S. A. Cummer, Electrical and Computer Engineering Department, Duke University, Box 90291, Durham, NC 27708, USA.

H. U. Frey and S. B. Mende, Space Sciences Laboratory, University of California, 7 Gauss Way, Berkeley, CA 94720-7450, USA.

H. Fukunishi and Y. Takahashi, Department of Geophysics, Tohoku University, Sendai 980-8578, Japan.

L. C. Lee, Institute of Space Science, National Central University, 300, Jhongda Road, Jhongli City, Taoyuan County 32001, Taiwan.